Full-disc ^{13}CO(1-0) mapping across nearby galaxies of the EMPIRE survey and the CO-to-H$_2$ conversion factor

D. Cormier[1,2]⋆, F. Bigiel[2], M. J. Jiménez-Donaire[2], A. K. Leroy[3], M. Gallagher[3],
A. Usero[4], K. Sandstrom[5], A. Bolatto[6], A. Hughes[7,8], C. Kramer[9], M. R. Krumholz[10],
D. S. Meier[11], E. J. Murphy[12], J. Pety[13,14], E. Rosolowsky[15], E. Schinnerer[16],
A. Schruba[17], K. Sliwa[16], F. Walter[16]

[1]*Laboratoire AIM, CEA/DSM - CNRS - Université Paris Diderot, Irfu/Service d'Astrophysique, CEA Saclay, F-91191 Gif-sur-Yvette, France*
[2]*Zentrum für Astronomie der Universität Heidelberg, Institut für theoretische Astrophysik, Albert-Ueberle-Str. 2, D-69120 Heidelberg, Germany*
[3]*Department of Astronomy, The Ohio State University, 140 W 18th Street, Columbus, OH 43210, USA*
[4]*Observatorio Astronómico Nacional, Alfonso XII 3, E-28014 Madrid, Spain*
[5]*Center for Astrophysics and Space Sciences, Department of Physics, University of California, San Diego, 9500 Gilman Drive, La Jolla, CA 92093*
[6]*Department of Astronomy and Laboratory for Millimeter-Wave Astronomy, University of Maryland, College Park, MD 20742, USA*
[7]*CNRS, IRAP, 9 Avenue Colonel Roche, BP 44346, F-31028 Toulouse cedex 4, France*
[8]*Université de Toulouse, UPS-OMP, IRAP, F-31028 Toulouse cedex 4, France*
[9]*Instituto de Radioastronomía Milimétrica, Av. Divina Pastora 7, Núcleo Central, E-18012 Granada, Spain*
[10]*Research School of Astronomy and Astrophysics, Australian National University, Canberra, ACT 2611, Australia*
[11]*Department of Physics, New Mexico Institute of Mining and Technology, 801 Leroy Place, Soccoro, NM 87801, USA*
[12]*National Radio Astronomy Observatory, 520 Edgemont Road, Charlottesville, VA 22903, USA*
[13]*Institut de Radioastronomie Millimétrique, 300 Rue de la Piscine, F-38406 Saint Martin d'Hères, France*
[14]*Observatoire de Paris, 61 Avenue de l'Observatoire, F-75014 Paris, France*
[15]*Department of Physics, University of Alberta, Edmonton, AB T6G 2E1, Canada*
[16]*Max-Planck-Institut für Astronomie, Königstuhl 17, D-69117 Heidelberg, Germany*
[17]*Max-Planck-Institut für extraterrestrische Physik, Giessenbachstrasse 1, D-85748 Garching, Germany*

ABSTRACT

Carbon monoxide (CO) provides crucial information about the molecular gas properties of galaxies. While ^{12}CO has been targeted extensively, isotopologues such as ^{13}CO have the advantage of being less optically thick and observations have recently become accessible across full galaxy discs. We present a comprehensive new dataset of ^{13}CO(1-0) observations with the IRAM 30-m telescope of the full discs of 9 nearby spiral galaxies from the EMPIRE survey at a spatial resolution of ∼1.5 kpc. ^{13}CO(1-0) is mapped out to $0.7 - 1\,r_{25}$ and detected at high signal-to-noise throughout our maps. We analyse the ^{12}CO(1-0)-to-^{13}CO(1-0) ratio ($\Re$) as a function of galactocentric radius and other parameters such as the ^{12}CO(2-1)-to-^{12}CO(1-0) intensity ratio, the 70-to-160 μm flux density ratio, the star-formation rate surface density, the star-formation efficiency, and the CO-to-H$_2$ conversion factor. We find that $\Re$ varies by a factor of 2 at most within and amongst galaxies, with a median value of 11 and larger variations in the galaxy centres than in the discs. We argue that optical depth effects, most likely due to changes in the mixture of diffuse/dense gas, are favored explanations for the observed $\Re$ variations, while abundance changes may also be at play. We calculate a spatially-resolved ^{13}CO(1-0)-to-H$_2$ conversion factor and find an average value of $1.0 \times 10^{21}\,\mathrm{cm}^{-2}\,(\mathrm{K\,km\,s}^{-1})^{-1}$ over our sample with a standard deviation of a factor of 2. We find that ^{13}CO(1-0) does not appear to be a good predictor of the bulk molecular gas mass in normal galaxy discs due to the presence of a large diffuse phase, but it may be a better tracer of the mass than ^{12}CO(1-0) in the galaxy centres where the fraction of dense gas is larger.

Key words: galaxies: spiral – galaxies: star formation – ISM: molecules.

⋆ E-mail: diane.cormier@cea.fr

1 INTRODUCTION

Since stars form out of the cold, dense regions of the interstellar medium (ISM) where conditions favor the presence of molecules, the low-level rotational transitions of ^{12}CO are commonly used to study star-formation properties in galaxies (e.g., Solomon & Sage 1988; Fukui & Kawamura 2010; Kennicutt & Evans 2012). CO has been extensively targeted because it is the most abundant molecule after molecular hydrogen (H_2) and cold H_2 cannot be observed directly in emission. CO starts to form at visual extinctions of 1-3 mag corresponding to column densities of $1-3\times10^{21}$ cm^{-2} at solar metallicity, while hydrogen becomes mostly molecular for column densities greater than a few 10^{20} cm^{-2}. Under normal metallicity and moderate radiation field conditions, most of the cold, dense ISM is not expected to be dark in CO, and CO and its rarer isotopologues are expected to trace well the H_2 column density of clouds (Tielens & Hollenbach 1985; van Dishoeck & Black 1988; Sternberg et al. 2014).

Over the past decades, the ^{12}CO(J=1-0) emission has been calibrated to provide a measure of the total mass of molecular hydrogen via the CO-to-H_2 conversion factor $X_{\rm CO}$ or $\alpha_{\rm CO}$ (e.g., Bolatto et al. 2013). In external galaxies, the main calibration techniques employed are based on the virial method, dust emission, optically thin molecular tracers, or radiative transfer of multiple molecules/transitions. These techniques often rely on making strong assumptions regarding, e.g., abundances, grain properties, filling factors, or the virialisation of molecular clouds. In addition, dependencies of the $X_{\rm CO}$ factor on physical conditions within clouds, such as density, temperature, turbulence or metallicity are expected (e.g., Wolfire et al. 2010; Shetty et al. 2011; Narayanan et al. 2011). As a consequence, the $X_{\rm CO}$ factor varies, as seen from galaxy to galaxy and across individual galaxies in observations (e.g., Arimoto et al. 1996; Downes & Solomon 1998; Leroy et al. 2011; Papadopoulos et al. 2012; Sandstrom et al. 2013; Cormier et al. 2014; Kamenetzky et al. 2014). In normal, star-forming disc galaxies, the amplitude of those variations is up to an order of magnitude (Bolatto et al. 2013; Sandstrom et al. 2013).

In addition to environmental dependencies of a luminosity-mass conversion factor, the high abundance and densities of ^{12}CO makes the $J = (1 - 0)$ transition optically thick in most molecular clouds, which complicates interpretation and can hamper accurate determination of cloud properties. Rarer isotopologues of the most abundant molecules containing carbon, such as ^{13}CO, are on the one hand less abundant and hence more difficult to observe in galaxies. On the other hand, they have the advantage of being more optically thin, allowing us to access the full column density of the material they arise from. Beyond our Galaxy (see Heyer & Dame 2015, for a review), ^{13}CO has mainly been observed in the centres or in small, targeted regions of nearby galaxies or integrated over entire, bright galaxies (e.g., Encrenaz et al. 1979; Young & Sanders 1986; Casoli et al. 1992; Aalto et al. 1995; Wilson et al. 1997; Paglione et al. 2001; Krips et al. 2010; Tan et al. 2011; Danielson et al. 2013; Alatalo et al. 2015; Vila-Vilaro et al. 2015; Sliwa et al. 2017a,b). With the "EMIR Multiline Probe of the ISM Regulating Galaxy Evolution" survey (EMPIRE; Bigiel et al. 2016), we have obtained complete and high signal-to-noise maps of ^{13}CO as well as the main dense molecular gas tracers (HCN, HCO$^+$, HNC) in the $J = 1 \rightarrow 0$ transition across the discs of nine nearby spiral galaxies with the IRAM 30-m telescope (Bigiel et al. 2016; Jiménez-Donaire et al. 2017b,c; Gallagher et al. 2017). We also obtained full maps of ^{12}CO(1-0) emission for those nine galaxies in follow-up programs. These galaxies are drawn from the HERACLES ^{12}CO(2-1) survey (Leroy et al. 2009). They are selected to have diverse structural properties (barred/unbarred, flocculent/grand-design spiral arms) and to reside in different environments (field/Virgo Cluster galaxy) in order to test whether these parameters influence their observable ISM properties.

In this paper, we present an analysis of the ^{13}CO(1-0) and ^{12}CO(1-0) observations from EMPIRE. Since ^{13}CO has not been observed or mapped as extensively as ^{12}CO in galaxies, our goal is to investigate variations in the ^{12}CO(1-0)-to-^{13}CO(1-0) ratio among and within those galaxies, and to understand if/under which conditions ^{13}CO may be a better tracer of the molecular gas mass than ^{12}CO. Throughout this paper, the ^{12}CO(1-0)-to-^{13}CO(1-0) integrated intensity ratio is denoted $\mathfrak{R}$. Section 2 describes the observations. Section 3 presents an analysis of $\mathfrak{R}$ with radial profiles and correlation diagrams, as well as a qualitative comparison to models and a derivation of column densities. The physical origin of $\mathfrak{R}$ variations and the ability of the CO lines to trace the molecular gas mass are discussed in section 4. Finally, we summarize our conclusions in section 5.

2 OBSERVATIONS

2.1 EMPIRE observations of ^{13}CO(1-0)

2.1.1 Data reduction

Observations of the IRAM 30-m large program EMPIRE (PI Bigiel) were carried out in 2012 (pilot program for NGC 5194) and between December 2014 and December 2016 (program 206-14, for the other galaxies). We mapped the full discs of 9 nearby spiral galaxies with the EMIR E0 receiver in the on-the-fly mapping mode. The half-power beam width (HPBW) at 110 GHz is 22 arcsec and the adopted spectral resolution is 4 km s^{-1}.

The data were reduced with our in-house pipeline. The main steps include: baseline subtraction with a polynomial function of order 2, rejection of spectra above 3 times the theoretical noise, conversion to main beam temperature assuming main beam and forward efficiencies of 0.78 and 0.94, projection of the spectra onto grids of pixel size 4 arcsec. After gridding, the full width half-maximum (FWHM) of the ^{13}CO(1-0) data is 27 arcsec. This corresponds to a linear resolution of ~1.5 kpc for our sample of galaxies. We refer to Jiménez-Donaire et al. (2017c,a) for a detailed description of the data acquisition and reduction. Line calibrators were observed during each run of the campaign and their intensities vary by about 5 per cent only. Table 1 provides the list of our targets and noise levels achieved at the frequency of the ^{13}CO(1-0) line (110.20 GHz).

2.1.2 Moment maps

We used the ^{12}CO(2-1) data from HERACLES (Leroy et al. 2009) as a guide to create integrated intensity maps for the ^{13}CO(1-0) line. The data were retrieved from the HER-ACLES repository[1], convolved to a common resolution of 27 arcsec using Gaussian kernels, and put on the same spatial grid as the EMPIRE data using the IDL procedure **has-trom**. At each position in the map, we fitted the ^{12}CO(2-1) line with a single Gaussian. For pixels below a signal-to-noise ratio of 5 for the velocity-integrated intensity, we interpolated central velocities and line widths from well-detected neighboring pixels by fitting a plane to the maps. In regions where most pixels are not detected in ^{12}CO(2-1), the interpolated central velocities are not allowed to take values lower (higher) than the minimum (maximum) velocity measured in the well-detected pixels, and the interpolated line widths are set to the average line width measured in the well-detected pixels.

The central velocities and line widths of the ^{12}CO(2-1) line were used as initial guesses for those of the ^{13}CO(1-0) line. We created intensity maps for ^{13}CO(1-0) both by fitting and integrating a single Gaussian and by integrating directly the signal in specific velocity windows. We defined the windows as $\sim 3\times$ FWHM of the ^{12}CO(2-1) line, thus the windows vary for each line of sight. The two methods yield differences in integrated intensities that are typically less than 7 per cent. Since the CO line profiles are not always Gaussian, especially in the galaxy centres, we prefer to use the direct integration maps and not the line-fitted maps. We also produced error maps. For each pixel, the error on the integrated intensity is calculated as the standard deviation in the line-free parts of each spectrum, multiplied by the square root of the number of $(4\,\mathrm{km\,s^{-1}}$ wide) channels inside the FWHM given by the Gaussian fit. Figure A1 in the Appendix shows final integrated intensity maps for each galaxy.

2.2 Ancillary data

2.2.1 Reference ^{12}CO data

In order to make homogeneous and matched-quality measurements of $\mathfrak{R}$, we performed new observations of 8 galaxies of the EMPIRE survey (all except NGC 5194) in the ^{12}CO(1-0) line, with the IRAM 30-m telescope. Maps of the entire discs were obtained as part of the programs 061-15, 059-16 (PI Jiménez-Donaire) and D15-12 (PI Cormier). The data were reduced with the same pipeline as for EM-PIRE and we produced final cubes at a spatial resolution of $\simeq 25$ arcsec and a spectral resolution of $4\,\mathrm{km\,s^{-1}}$. We reached sensitivities of 17-30 mK (T_{mb}) per $4\,\mathrm{km\,s^{-1}}$ channel. For NGC 5194, the ^{12}CO(1-0) and ^{13}CO(1-0) data are taken from the PAWS survey (30-m cubes[2]; Schinnerer et al. 2013; Pety et al. 2013).

All datasets are convolved to a common resolution of 27 arcsec using Gaussian kernels and put on the same spatial grid as the EMPIRE data. Integrated intensity maps are created following the same steps as for the ^{13}CO(1-0) data, described in section 2.1.2.

2.2.2 Ultraviolet and infrared photometry

All of the EMPIRE targets were observed with GALEX as well as with the MIPS instrument onboard *Spitzer* as part of the programs LVL (Dale et al. 2009) and SINGS (Kennicutt et al. 2003). *Herschel* photometry exists for all of our targets except NGC 2903. We use user-provided products from the key programs VNGS and KINGFISH (data release 3) (Bendo et al. 2012; Kennicutt et al. 2011). No PACS $100\,\mu$m observations are available for NGC 5194. The reduction and map-making were done in HIPE versions 9 and 8 and Scanamorphos versions 21 and 16.9, respectively. Convolutions are done using the kernels from Aniano et al. (2011).

2.3 Deriving physical quantities

2.3.1 Σ_{SFR}, Σ_{mol}, $N(\mathrm{H_2})$

From the photometry and spectroscopy, we derive physical quantities such as star-formation rate surface densities (Σ_{SFR}), molecular gas surface densities (Σ_{mol}), and H_2 column densities ($N(\mathrm{H_2})$). All surface densities are corrected for inclination.

Our SFR estimates are based on IR data. For all galaxies overlapping with KINGFISH, we use the TIR maps calculated with dust models from Galametz et al. (2013). For NGC 5194 and NGC 2903, we compute TIR surface brightness using the generic calibration from Galametz et al. (2013). We combine the bands MIPS $24\,\mu$m, PACS 70, $160\,\mu$m and SPIRE $250\,\mu$m for NGC 5194 and the bands MIPS 24 and $70\,\mu$m for NGC 2903. For the galaxies in KING-FISH, the comparison of TIR maps calculated from SED models and from the generic calibration yield differences of about 10 per cent for the first combination (MIPS, PACS and SPIRE) and 20 per cent for the second combination (MIPS only). The generic calibration tends to systematically overpredict slightly the TIR flux in the brightest regions. Uncertainty maps are generated by adding in quadrature errors on the fluxes and errors on the calibration coefficients and from the choice of method as quoted above in the case of the TIR calibration. The TIR maps are then converted to star-formation rate surface density maps using the calibration from Murphy et al. (2011).

Molecular gas mass surface densities and H_2 column densities are commonly derived using the ^{12}CO(1-0) line as a proxy for H_2 and a CO-to-H_2 conversion factor. For Σ_{mol}, the standard conversion factor is α_{CO} of 4.4 $M_\odot$ $\mathrm{pc^{-2}\,(K\,km\,s^{-1})^{-1}}$ which includes helium (Bolatto et al. 2013). For $N(\mathrm{H_2})$, the standard conversion factor is X_{CO} of 2×10^{20} $\mathrm{cm^{-2}\,(K\,km\,s^{-1})^{-1}}$ which does not account for helium. These are considered as reference, Milky-Way values. Variations of the conversion factors are discussed in section 4.2.

2.3.2 Isotope abundance ratio and ^{12}CO abundance

The ^{12}C/^{13}C isotope abundance ratio results from stellar processing and evolution (e.g., Wilson & Rood 1994).

Table 1. General properties of the EMPIRE galaxies.

Name	Type	RA (J2000)	Dec (J2000)	Dist (Mpc)	D_{25} (arcmin)	i (deg)	PA (deg)	$\sigma_{\rm rms}$ (mK)	I_{13} (K km s^{-1})	Map size (arcmin^2)
NGC 0628	SAc	01:36:41.8	15:47:01	9.6	9.8	7	20	4.8	0.25 ± 0.01	4.5×4.5
NGC 2903	SABbc HII	09:32:10.1	21:30:04	8.9	11.8	65	204	3.5	1.27 ± 0.01	2.4×4.1
NGC 3184	SABcd group	10:18:17.0	41:25:28	11.8	7.4	16	179	3.8	0.36 ± 0.01	3.5×3.5
NGC 3627	SABb liner AGN	11:20:15.0	12:59:30	9.4	10.3	62	173	4.4	1.24 ± 0.01	2.9×5.2
NGC 4254	SAc HII	12:18:49.6	14:24:59	14.4	5.0	32	55	3.0	0.87 ± 0.01	3.4×3.2
NGC 4321	SABbc AGN	12:22:54.9	15:49:21	14.3	6.0	30	153	3.6	0.91 ± 0.01	4.3×2.9
NGC 5055	SAbc liner AGN	13:15:49.2	42:01:45	7.9	11.9	59	102	4.6	1.02 ± 0.01	6.4×3.5
NGC 5194	SAbc Seyfert 2	13:29:52.7	47:11:43	7.6	7.7	20	172	4.5	1.07 ± 0.01	6.8×6.8
NGC 6946	SABcd HII	20:34:52.2	60:09:14	6.8	11.4	33	243	4.6	0.88 ± 0.01	6.3×5.3

Notes. See Jiménez-Donaire et al. (2017b) for references on the galaxy parameters. The distance to NGC 0628 has been updated to the value from Kreckel et al. (2017). Morphological types are from the NASA Extragalactic Database. Column 9: rms noise in the ^{13}CO(1-0) data, calculated as the median noise level at the rest frequency of 110.2 GHz, for a spectral resolution of 4 km s^{-1} and spatial resolution of 27 arcsec. Column 10: average ^{13}CO(1-0) integrated intensity and its statistical uncertainty measured by stacking all spectra across the entire map size given in Column 11.

The ^{12}CO/^{13}CO abundance ratio further depends on chemical processes within molecular clouds. While we discuss possible sources of variations in those abundances in section 4, in our analysis we make no difference between the isotope (^{12}C/^{13}C) abundance ratio and the isotopologue (^{12}CO/^{13}CO) abundance ratio. The abundance ratio is largely unconstrained for external galaxies but has been observed to vary within galaxies and from galaxy to galaxy. In the Milky Way, it increases from 25 in the centre to 100 in the outer disc, with a value of ~70 in the solar neighborhood (Langer & Penzias 1990; Wilson & Rood 1994; Milam et al. 2005). In the Large Magellanic Cloud, it is ~50 (Wang et al. 2009). In starburst galaxies, it is found to be >40, and in some ULIRGs it is even > 100 (e.g., Martín et al. 2010; Henkel et al. 2014; Sliwa et al. 2017b). Here, we adopt a fiducial value for the isotope abundance ratio of 60. In the Milky Way, this value corresponds to a distance of $\simeq 6.7$ kpc or $0.6 r_{25}$.

The ^{12}CO/H$_2$ abundance ratio is also sensitive to radiative processes and gas chemistry. It can vary by orders of magnitudes from translucent to dense lines-of-sight, with a typical scatter of 0.5 dex at any given H$_2$ column density (van Dishoeck et al. 1992; Sheffer et al. 2008). In our large telescope beam, such different lines of sights are mixed and beam-to-beam variations of the abundance are expected to be smaller. In the following, we take the canonical value of 10^{-4} for the ^{12}CO/H$_2$ abundance ratio, which corresponds to a ^{13}CO/H$_2$ abundance ratio of 1.7×10^{-6} (e.g., Dickman 1978) and could be uncertain by a factor of a few.

3 ANALYSIS

3.1 ^{13}CO(1-0) intensities across galaxies

Figure 1 shows the ^{13}CO(1-0) and scaled ^{12}CO(1-0) intensities as a function of the PACS 70 μm intensity, which can be seen as a proxy of the star-formation rate surface density, as well as histograms of the ^{13}CO(1-0) intensities for each galaxy. ^{13}CO(1-0) is detected throughout our maps with signal-to-noise ratio > 10 in the brightest regions, and the majority of the pixels in our maps are detected at a

> 5σ level. ^{13}CO(1-0) peaks on the galaxy centres, except in NGC 3627 where it peaks on the star-forming knots at the end of the bar (though this may be somewhat an artifact of resolution). In the inter-arm/outer-disc regions, the ^{13}CO(1-0) intensity has values <1 K km s^{-1} (<0.3 K km s^{-1} for the two faintest galaxies NGC 0628 and NGC 3184).

We quantify correlations with the Spearman's rank correlation coefficient and its significance using the IDL procedure `r_correlate.pro`. The correlation coefficient is computed for data points with signal-to-noise ratio of the ^{13}CO(1-0) intensity greater than 5. With this condition, the signal-to-noise of the ancillary data sets described above is generally not a concern. The significance corresponds to the p-value or probability of null hypothesis. It is reported in parenthesis in the figures. The uncertainty (±) on the coefficient is estimated with a Monte-Carlo simulation. We find that ^{13}CO(1-0) and ^{12}CO(1-0) are generally well correlated with the dust emission from PACS 70 μm. Both CO lines show very similar distributions and scatter, with departure from each other in some galaxy centres (e.g., NGC 5055). At the resolution of our data, their line profiles and line widths are also similar (see Fig. A3).

Given the high quality of the data, we perform a line-of-sight based analysis. Only in the following section 3.2, we perform a stacking analysis to extract representative spectra in the different environments of our sample of galaxies.

3.2 $\Re$ in the different environments of spirals

$\Re$ is the ratio of the ^{12}CO(1-0) intensity and the ^{13}CO(1-0) intensity, which have units of K km s^{-1}. We measure $\Re$ in the galaxy centres, arm, inter-arm regions and total emission in our maps by means of stacking. In the stacking step, spectra corresponding to a given region are aligned in velocity using the ^{12}CO(2-1) data as reference and averaged. Jiménez-Donaire et al. (2017b) describes the method in detail and Figure A3 shows stacked spectra of ^{13}CO(1-0) and ^{12}CO(1-0) for the galaxy centres and entire galaxies. CO intensities are then measured by direct integration of the stacked spectra over a velocity window large enough to encompass all the signal. Table 2 reports the $\Re$ values ob-
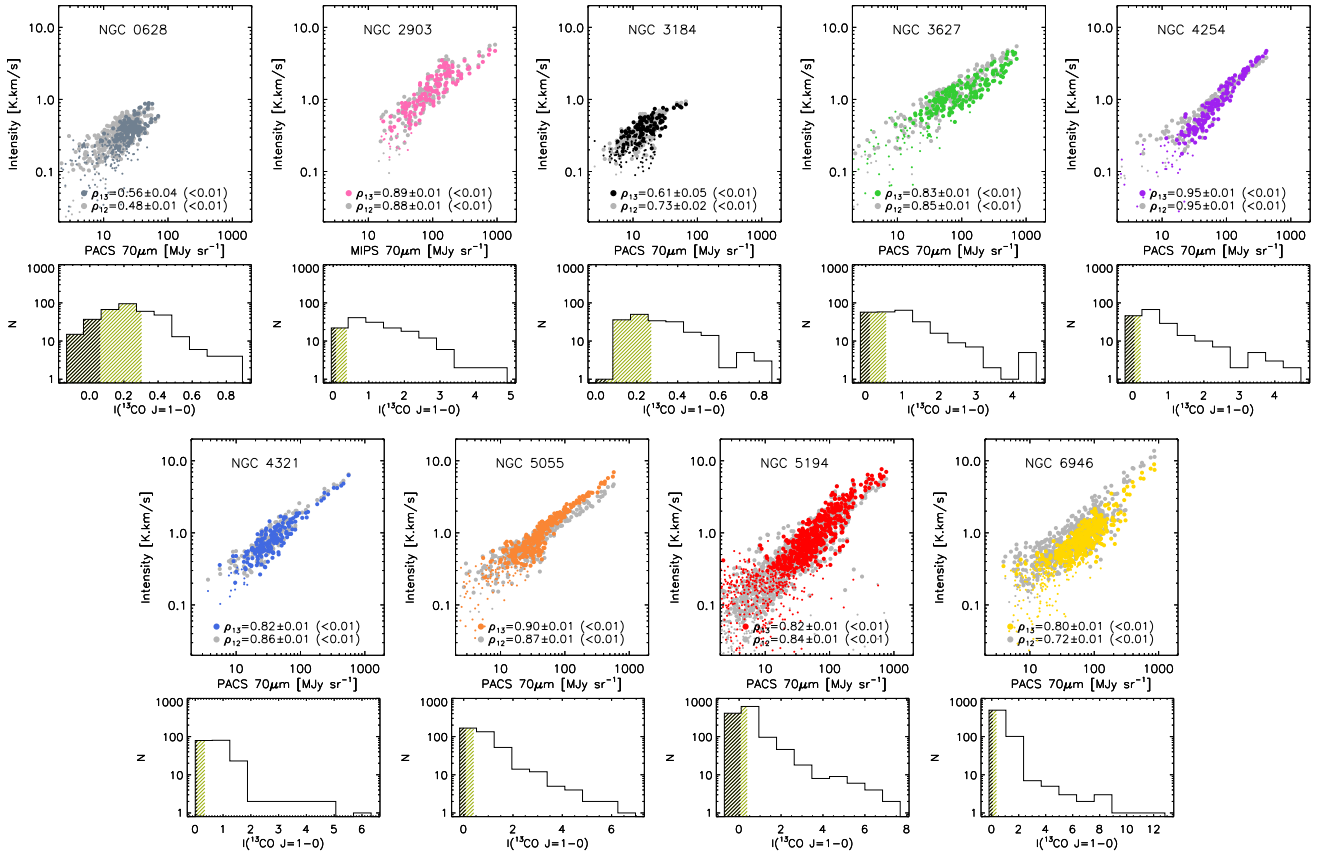
Figure 1. Top panels: EMPIRE observations of the CO line intensity (in $K\,km\,s^{-1}$) on the y-axis following well the broadband $70\,\mu m$ intensity (in $MJy\,sr^{-1}$) which is a proxy for the star-formation rate surface density on the x-axis. $^{13}CO(1-0)$ data are in colour and $^{12}CO(1-0)$ data, scaled by a factor of 10, are in grey. For both CO lines, smaller circles correspond to pixels below a signal-to-noise ratio of 5 in the respective maps. The Spearman's rank correlation coefficients between each CO line intensity and the $70\,\mu m$ intensity, their uncertainty, and their significance (in parenthesis), are indicated. Those are measured on data with signal-to-noise ratio above 5. Bottom panels: Histogram of the $^{13}CO(1-0)$ intensities. Only few pixels are below the 1σ (5σ) noise level as indicated by the hashed black (beige) parts of the histograms.

tained this way for each galaxy as well as averages and dispersions over the sample. Figure A1 in the Appendix shows maps of $\mathfrak{R}$ with contours delineating the centre and arm regions. The regions were defined using cuts in intensity of the $^{12}CO(1-0)$ line (at our working resolution of $27\,arcsec$ or $\simeq 1.5\,kpc$), and the cut levels were chosen by eye. 'Centre' refers to the galaxy centres (distance to the centre of the galaxy $<16\,arcsec$ or inner $0.8\,kpc$, typically) where the $^{12}CO(1-0)$ emission is brightest (first cut at CO intensity levels of: 5.5, 35, 7, 30, 32, 22, 30, 32, 40 $K\,km\,s^{-1}$, for NGC 0628, 2903, 3184, 3627, 4254, 4321, 5055, 5194, 6946, respectively). 'Arm' refers to the galaxy discs where the $^{12}CO(1-0)$ emission is bright (second cut at CO intensity levels of: 3, 18, 3.5, 11, 11, 8, 10, 10, 10 $K\,km\,s^{-1}$, for NGC 0628, 2903, 3184, 3627, 4254, 4321, 5055, 5194, 6946, respectively). 'Inter-arm' refers to the inter-arm and outer parts of the maps where the $^{12}CO(1-0)$ emission is fainter but detected at a signal-to-noise ratio > 3. Finally, 'total' refers to the entire map where $^{12}CO(1-0)$ is detected. We note that we also defined contours by hand, identifying centres and arm regions based on $24\,\mu m$ and $70\,\mu m$ continuum images. Values of $\mathfrak{R}$ obtained by stacking with these hand contours vary by at most 10 per cent compared to values reported in Table 2.

This 10 per cent discrepancy can be seen as a methodology uncertainty.

Thanks to our sensitive, full maps, we can achieve much better galaxy-integrated and environment-specific measurements than previous investigations of $\mathfrak{R}$ in nearby galaxies. In all galaxies and all environments, the noise of the data indicates that we could have measured ratios up to 150 in the stacks (but the observed ratios are much lower). The mean global (i.e. full-galaxy) $\mathfrak{R}$ value that we measure over our sample is 11 with a standard deviation of 1.5. When the galaxies are divided into different environments (centre, arm, inter-arm regions), we obtain similar average $\mathfrak{R}$ values, with standard deviation ~2. We notice that the dispersion in $\mathfrak{R}$ is highest in the galaxy centres, with values varying between 7 and 15 (see Table 2). The dispersion is also high in the inter-arm regions, but with larger error bars on individual measurements. Studying, also at a kpc-scale, centres of ~10 nearby galaxies with AGN activity, signs of a recent merger, or an intense central starburst, Israel (2009a,b) found values of $\mathfrak{R}$ in the range $8-16$. In the EMPIRE survey, we find that the galaxies with bright, starburst-dominated nuclei (NGC 2903, NGC 3627, NGC 4321, and NGC 6946) have the largest central $\mathfrak{R}$ values. Two galaxies in our sample have strong bars (NGC 2903

Table 2. $\mathfrak{R}$ values in different regions of spirals.

Name	$\mathfrak{R}_{\text{total}}$	$\mathfrak{R}_{\text{centre}}$	$\mathfrak{R}_{\text{arm}}$	$\mathfrak{R}_{\text{inter-arm}}$
NGC 0628	13.2 ± 0.6	9.9 ± 0.4	13.5 ± 0.7	14.4 ± 1.6
NGC 2903	10.3 ± 0.1	12.3 ± 0.3	11.0 ± 0.1	9.4 ± 0.2
NGC 3184	10.2 ± 0.3	11.2 ± 0.7	10.7 ± 0.4	9.3 ± 0.5
NGC 3627	12.0 ± 0.1	15.2 ± 0.5	12.2 ± 0.1	10.8 ± 0.4
NGC 4254	11.0 ± 0.2	8.4 ± 0.1	10.5 ± 0.1	13.3 ± 0.5
NGC 4321	10.3 ± 0.2	10.9 ± 0.1	10.3 ± 0.2	9.8 ± 0.3
NGC 5055	9.3 ± 0.2	7.2 ± 0.1	8.5 ± 0.2	10.9 ± 0.4
NGC 5194	10.3 ± 0.3	8.2 ± 0.1	9.9 ± 0.1	12.8 ± 0.9
NGC 6946	13.8 ± 0.2	15.2 ± 0.1	13.5 ± 0.2	13.2 ± 0.4
average all	11.2 (1.5)	10.9 (2.9)	11.1 (1.7)	11.5 (1.9)
average nuc.[a]	11.6 (1.7)	13.4 (2.2)	11.8 (1.4)	10.8 (1.7)

Notes. The *inter-arm* region refers to the entire map disregarding the centre and the arms, i.e. [*total* − (*centre* + *arms*)]. Errors on the stacked values of $\mathfrak{R}$ correspond to statistical errors. For averages, we indicate the standard deviation of $\mathfrak{R}$ in parenthesis. (*a*) Only galaxies with nuclear starbursts (NGC 2903, NGC 3627, NGC 4321, and NGC 6946).

and NGC 3627) and three other galaxies have weaker bars (NGC 3184, NGC 4321, NGC 6946, and possibly NGC 5194). Those barred galaxies also show generally higher central $\mathfrak{R}$ values than the non-barred galaxies. Both properties of having a bar and a starburst-dominated nucleus might be related as bars may help to funnel gas towards the galaxy center – leading to high dense gas fractions (Gallagher et al. 2017) – and to fuel star formation (e.g., Ho et al. 1997). Finally, two galaxies with AGN activity have low central $\mathfrak{R}$ values (NGC 5055, NGC 5194) but the trend is not systematic (e.g., NGC 3627 also has AGN activity).

3.3 Radial Profiles

3.3.1 Method

We generate radial profiles for the main tracers discussed in this paper: ^{13}CO(1-0), ^{12}CO(1-0), and ^{12}CO(2-1). We choose a step size in radius of 13.5 arcsec, corresponding to half of the spatial resolution. At a given radius, we measure the average of the intensities within a tilted ring. The width of the rings is taken as the chosen step size (defined along the minor axis), so that the rings are not overlapping, but they are correlated because the beam is oversampled. Table 1 gives the assumed inclinations and position angles. Error bars on those measurements are calculated as the root-mean-squared error within each ring of our error maps and multiplied by the square root of the oversampling factor N_s, defined as $N_s = 1.13 \times (\text{map resolution/pixel size})^2$. All intensity profiles are multiplied by $cos(i)$ to correct for inclination. Profiles of intensity ratios, such as $\mathfrak{R}$, are built by dividing the radial profile of the quantity at the numerator with the radial profile of the quantity in the denominator. Figure A2 shows radial profiles of the individual CO line intensities for each galaxy and Figure 2 shows radial profiles of $\mathfrak{R}$ for all galaxies.

3.3.2 Description of the profiles

Radial profiles of ^{13}CO(1-0), ^{12}CO(1-0), and ^{12}CO(2-1) globally follow each other very well for all galaxies (Fig. A2). Intensities peak in the centre and decrease by an order of magnitude at $r \simeq 0.6 \, r_{25}$, and even more for NGC 6946 which has a very prominent centre.

Differences in the radial behavior of ^{13}CO(1-0) and ^{12}CO(1-0) are made more obvious by inspecting $\mathfrak{R}$ (Fig. 2). We have reliable measurements of $\mathfrak{R}$ out to $r \simeq 8 \, \text{kpc}$ or $r \simeq 0.7 \, r_{25}$.

• The profiles of $\mathfrak{R}$ in NGC 2903, NGC 3627, and NGC 6946 decrease by a factor $1.2 - 1.4$ from centre to disc ($r = 3 \, \text{kpc}$) and stay mostly flat at larger radii. For NGC 3627, we notice a clear suppression of the ^{13}CO(1-0) peak intensities in the galaxy centre (see Figures A1 and A2 in the Appendix).

• The profiles of NGC 3184 and NGC 4321 are flat at all radii.

• The profiles of NGC 4254, NGC 5194, and NGC 5055 increase steadily by a factor of 1.4 from centre to outer disc ($r \simeq 7 \, \text{kpc}$).

• The profile of NGC 0628 is peculiar. It increases by a factor of 1.8 from centre to $r = 2 \, \text{kpc}$ and stays mostly flat at larger radii.

Centres aside, we find that the profiles increase slightly as a function of radius on average. The increase is mild compared to that observed in the Milky Way (Roman-Duval et al. 2016). At large radii ($r = 7 - 8 \, \text{kpc}$), our sample of galaxies and the Milky Way have similar $\mathfrak{R}$ values, but at lower radii, the Milky Way shows systematically lower values, between 5 and 8. $\mathfrak{R}$ increases by a factor of ~ 2 from the inner disc to the outer disc of the Milky Way. Such measurements, along with observations of rarer isotopologues of CO, have been used to infer abundance gradients in the Milky Way (Milam et al. 2005, shown as the black dotted line in Fig. 2). $\mathfrak{R}$ profiles are different in our sample of galaxies, implying that the Milky Way as a massive, rather quiescent galaxy (e.g., Chomiuk & Povich 2011) that may be compact for its stellar mass, might represent a different physical regime than the galaxies in our survey (e.g., different abundance patterns), or that there could be issues (e.g., geometric) in comparing Milky Way and extragalactic work. For example, the study of Roman-Duval et al. (2016) was limited to regions less than 50 pc away from the Galactic plane and it could be missing substantial ^{12}CO emission at high latitude (Dame et al. 2001) that we do capture in our sample.

3.3.3 Comparison to the literature on nearby spirals

Paglione et al. (2001) observed ^{13}CO(1-0) and ^{12}CO(1-0) along the major axes of NGC 3184, NGC 3627, NGC 5055, NGC 5194 and NGC 6946 with the FCRAO 14-m telescope (beam size ~47 arcsec). Their central and outer values globally agree with our observations within errors, except for NGC 3184 for which Paglione et al. (2001) find $\mathfrak{R}$ values two times lower but with marginal detections. For NGC 3627, we find a lower average in the disc (12 instead of 17), but they have much lower statistics. For NGC 6946, we find similar central values but larger values in the disc (13-14 instead of
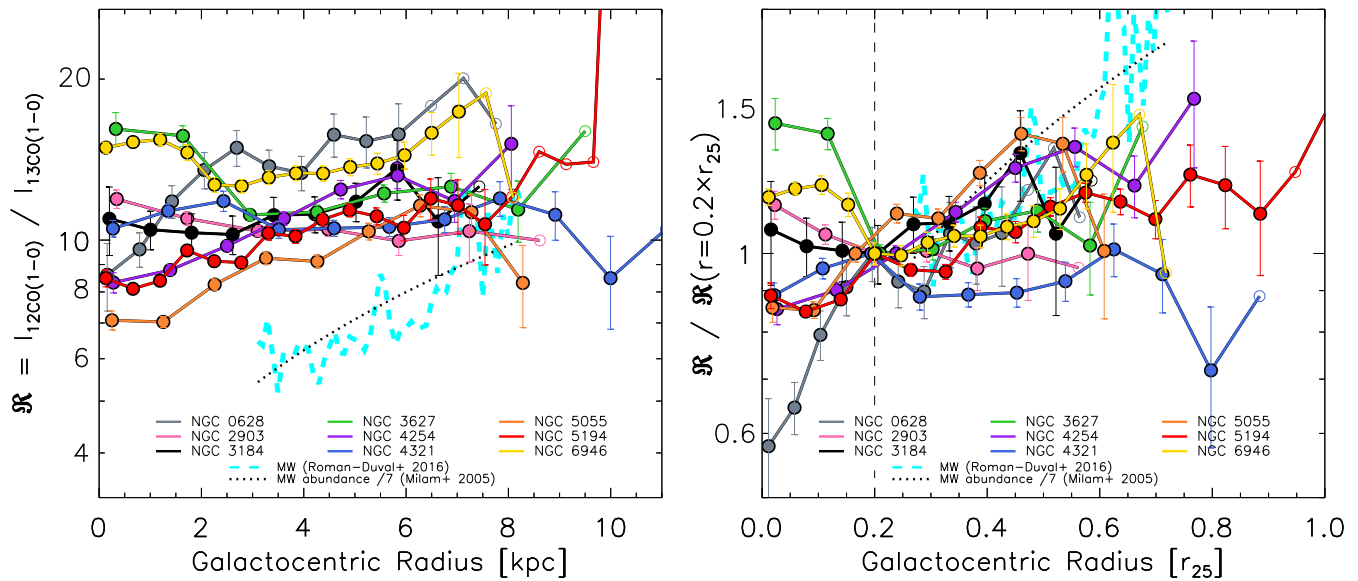
Figure 2. Left panel: Profiles of the ^{12}CO(1-0)-to-^{13}CO(1-0) intensity ratio, $\Re$, as a function of galactocentric radius for each EMPIRE galaxy. Profile points for which the average ^{13}CO(1-0) or ^{12}CO(1-0) intensity within the ring is below 5σ are shown with open circles. We overlay for reference the Milky Way measurements of the $\Re$ profile (dashed cyan curve) from Roman-Duval et al. (2016) and of the ^{12}C/^{13}C abundance gradient (black dotted line, divided by a factor of 7 for display) from Milam et al. (2005). Right panel: same as the left panel with radii normalized to r_{25} (x-axis) and the profiles normalized to their value at a radius of $r = 0.2\,r_{25}$. We assume $r_{25} = 11.5$ kpc for the Milky Way (de Vaucouleurs & Pence 1978).

10). At high resolution (5 arcsec or ~150 pc), Meier & Turner (2004) find a range of values between 7-20 in the nucleus of NGC 6946, which is compatible with our central average of 15. Muraoka et al. (2016) mapped NGC 2903 with the NRO 45-m telescope (beam size ~14 arcsec). They find values of $\Re$ that are around 10, which is globally consistent with our results. They divide the galaxy in ten distinct regions and find that $\Re$ varies by a factor of about two in the different environments. Although our resolution is coarser, we do not find as large spatial variations within NGC 2903 as they do. However, we achieve much better signal-to-noise ratios for individual ^{13}CO(1-0) measurements. Garcia-Burillo et al. (1993) mapped NGC 5194 with the IRAM 30-m and find similar values as Pety et al. (2013) (and therefore as us) in the centre and disc of this galaxy. Tosaki et al. (2002) also mapped part of the disc and the centre of NGC 5194 with the NRO telescope and found larger values (≥ 20) in the centre and inter-arm regions and attributed discrepancies in $\Re$ to differences in beam size ($\simeq 17$ arcsec versus $\simeq 25$ arcsec). In addition, Tan et al. (2011) observed the centre of NGC 2903 and Li et al. (2015) observed the centres of NGC 3184, NGC 3627, NGC 4254, and NGC 4321 with the PMO 14-m telescope (beam size ~55-60 arcsec). Both studies found $\Re$ values consistent with ours. Vila-Vilaro et al. (2015) also observed the centres of NGC 0628, NGC 2903, NGC 4254, and NGC 5055 with the ARO KP 12-m telescope (beam size ~56 arcsec). We find similar values as theirs, except for the centre of NGC 4254 (8 instead of 11.5). The discrepancy could be attributed to beam size differences, as we find a global average for NGC 4254 closer to 11, or to calibration uncertainties. Our value in the centre of NGC 4254 is closer to that reported by Li et al. (2015).

In high-resolution mapping observations of 23 nearby disc galaxies selected to lie on the blue sequence and to be actively star-forming, IR-bright galaxies (CARMA STING survey[3]), probing scales of $300-500$ pc, Cao et al. (2017) find similar $\Re$ ratios and flat $\Re$ profiles. They report that $\Re$ varies mostly from galaxy to galaxy, with values between 5 and 15. This behavior resembles what we find in the centres of our sample of galaxies, but our profiles in the discs show less scatter. While they are limited by sensitivity and focus on the inner bright, molecular gas-rich regions, we detect fainter and more diffuse regions with EMPIRE, enabling us to probe a wider range of environments (centre, arm, inter-arm regions). gal Sakamoto et al. (1997) performed strip-scan observations of the edge-on spiral NGC 891 at a resolution of 14 arcsec. They find a high value of $\Re \simeq 15$ in the centre and a general increase of $\Re$, from 4 at $r = 3$ kpc to 20 at $r = 10$ kpc. The increase of $\Re$ with radius is less pronounced in our sample of galaxies.

Overall, there is generally good agreement between our $\Re$ measurements and those reported in the literature for the EMPIRE galaxies or for similar types of galaxies and at similar scales. When there are discrepancies, these tend to be due to noise in the data. The uniqueness of the EMPIRE survey lies in the large, homogeneous spatial coverage (out to $r \simeq 0.5\,r_{25}$) and high signal-to-noise ratios achieved.

3.4 Correlation with tracers of star formation and ISM properties

In this section, we investigate how $\Re$ correlates with physical parameters such as the line ratio CO(2-1)/CO(1-0), the

---

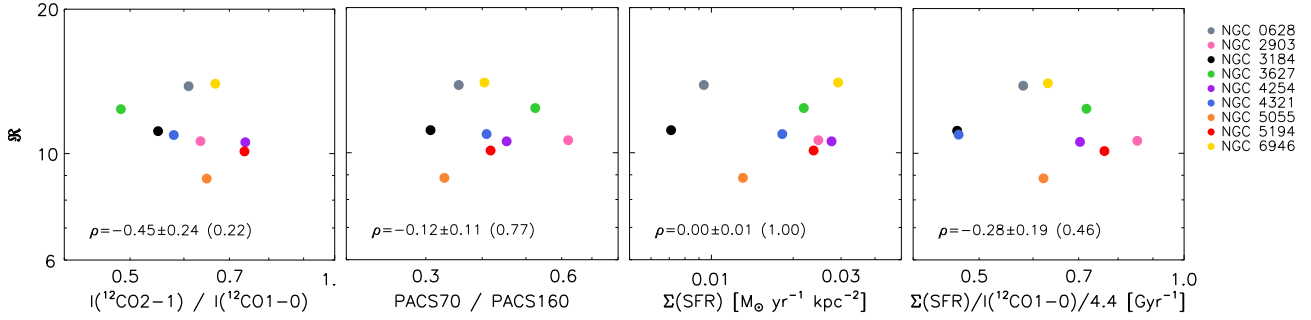[3] http://www.astro.umd.edu/~bolatto/STING/

Figure 3. Correlation between the $^{12}CO(1\text{-}0)$-to-$^{13}CO(1\text{-}0)$ intensity ratio $\mathfrak{R}$ and several quantities: the $^{12}CO(2\text{-}1)/^{12}CO(1\text{-}0)$ ratio probing the gas physical conditions, the PACS70/PACS160 flux density ratio probing the dust temperature, the star-formation rate surface density Σ_{SFR}, and the $\Sigma_{SFR}/CO(1\text{-}0)$ ratio which is a proxy for the star-formation efficiency. Quantities are averaged over entire galaxies and do not show significant correlations. Uncertainties on the galaxy averages are plotted but smaller than the symbol sizes. We also indicate the Spearman's rank correlation coefficients, their uncertainty, and their significance (in parenthesis).

Figure 4. (*a*) – Individual measurements of $\mathfrak{R}$ as a function of the $CO(2\text{-}1)/CO(1\text{-}0)$ intensity ratio. We show one panel per galaxy. The grey data correspond to all kpc-size data points with smaller symbol size for $^{13}CO(1\text{-}0)$ data with signal-to-noise ratio below 5. The binned values, in colour, consider all data points in the bin. We also indicate Spearman's rank correlation coefficients, their uncertainty, and their significance (in parenthesis), which are measured on data with signal-to-noise ratio above 5.

IR colour PACS70/PACS160, the star-formation rate surface density (Σ_{SFR}), and the $\Sigma_{SFR}/CO(1\text{-}0)$ ratio ($\propto$ star-formation efficiency). We use the $CO(2\text{-}1)/CO(1\text{-}0)$ ratio as a probe of gas conditions (temperature, density, opacity), and the IR colour PACS70/160 as an indicator of dust temperature that could be coupled to the gas temperature in the case where densities are high enough that collisions between dust grains and the gas particles lead to equal gas and dust temperatures.

Figure 3 shows values averaged over entire galaxies

while Figure 4 shows the individual ~kpc-sized regions as well as binned values for each galaxy. To produce these measurements, we first sample our maps with a hexagonal grid of spacing 13.5 arcsec (half of the spatial resolution). For total averages (Fig. 3), we measure the average of each observed quantity (CO intensity, PACS flux density, Σ_{SFR}, etc.) by considering all sampling points, and for ratios, we divide these averages with each other. For the bins, we construct irregular bins of the physical quantities such that each bin contains 20 sampling points. Similarly (Fig. 4), we measure
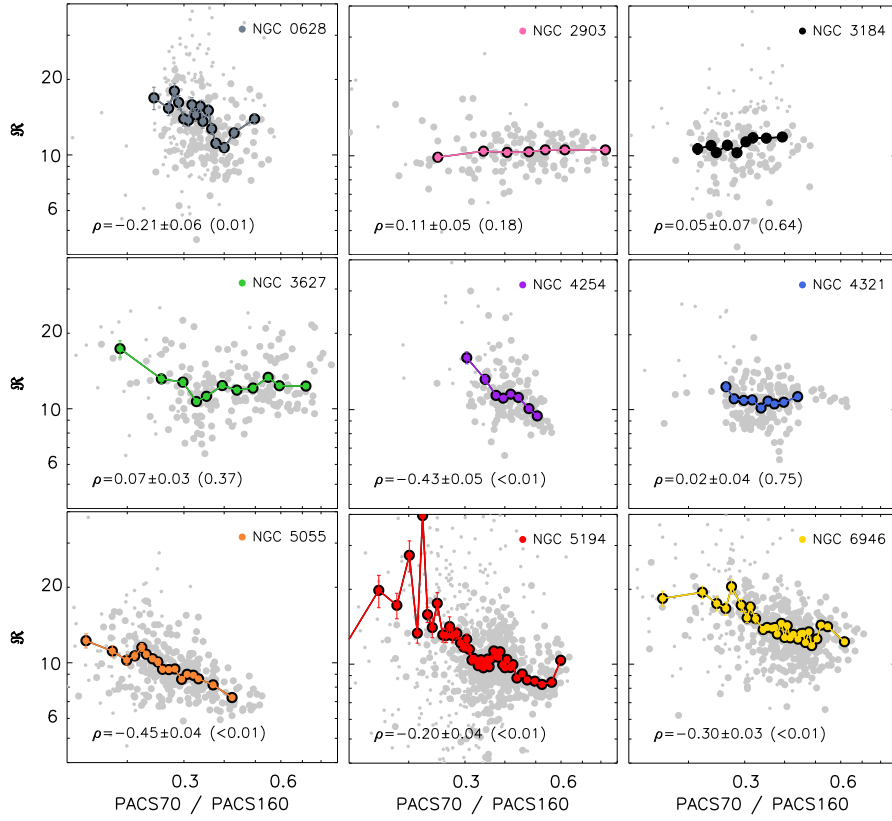
Figure 4 – *continued* (*b*) – Individual measurements of $\Re$ as a function of the PACS70/PACS160 flux density ratio. For NGC 2903, we use the MIPS70/MIPS160 flux density ratio.

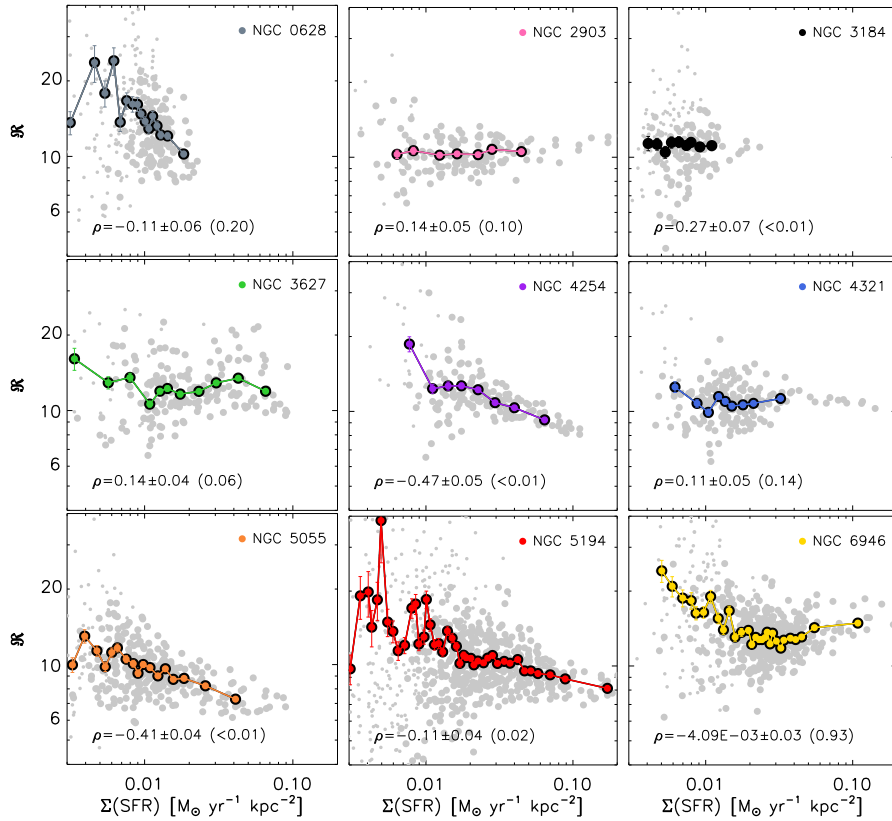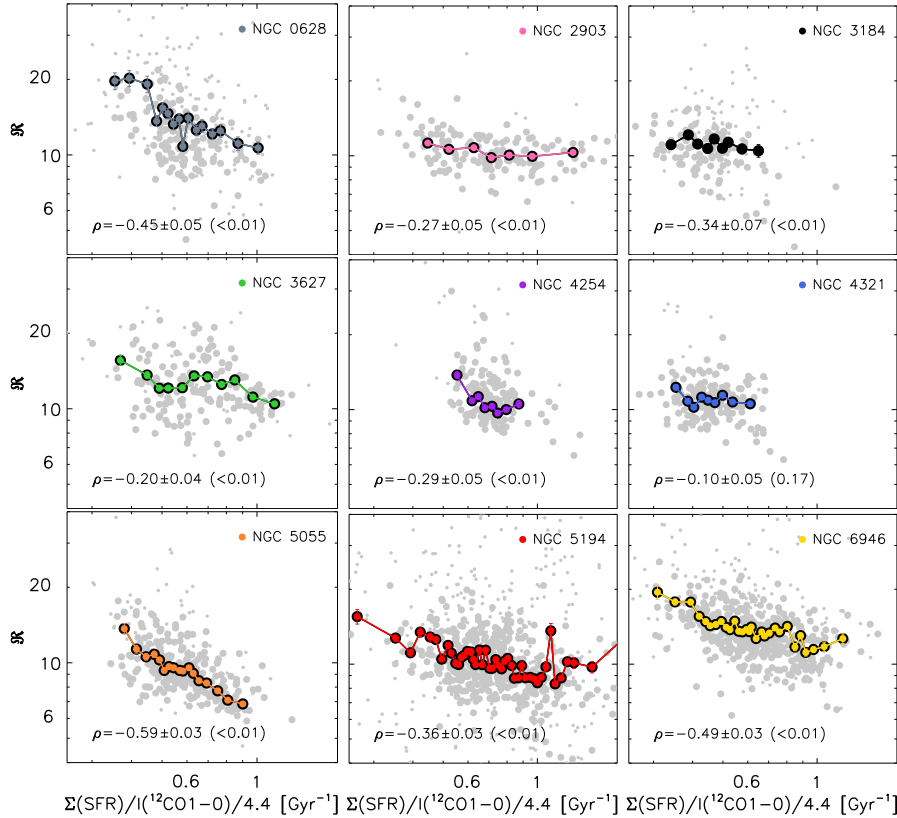**Figure 4** – *continued* (*c*) – Individual measurements of $\Re$ as a function of the star-formation rate surface density, Σ_{SFR}.

Figure 4 – *continued* (*d*) – Individual measurements of $\mathfrak{R}$ as a function of the Σ_{SFR}/CO(1-0) ratio ($\propto$ star-formation efficiency).

the intensity of each CO line and its error, either by considering the individual sampling points (for the kpc-size regions) or by averaging intensities of the sampling points falling in the bin (binned averages). We then calculate $\mathfrak{R}$ by taking the ratio of these intensities. We do not mask sampling points with low signal-to-noise when doing the binned averages. Error bars are calculated as the dispersion in $\mathfrak{R}$ measurements obtained with a Monte-Carlo simulation.

Inspecting Fig. 3, we find that the global averaged values of $\mathfrak{R}$ are not correlated with any quantity. Looking at integrated galaxies, Aalto et al. (1995) find that the warmest galaxies (F60/F100≥0.7), which are absent in our EMPIRE sample, display systematically high $\mathfrak{R}$ values (> 10), while $\mathfrak{R}$ and F60/F100 do not correlate for cold-intermediate IR colours (F60/F100≤0.6), which is in line with our results. Moreover, Davis (2014) report a correlation between $\mathfrak{R}$ and Σ_{SFR} for integrated early-type galaxies. The Σ_{SFR} range that they investigate is much larger than ours (5 orders of magnitude as opposed to a dynamic range in the average Σ_{SFR} of less than 1 dex in our case). This may be why we do not find a significant trend with Σ_{SFR}. We discuss Figure 4 in detail next.

CO(2-1)/CO(1-0) intensity ratio (Fig. 4a): We find that $\mathfrak{R}$ systematically decreases with increasing CO(2-1)/CO(1-0) ratio within galaxies. Moreover, for a given value of CO(2-1)/CO(1-0), there are significant offsets in $\mathfrak{R}$ from galaxy to galaxy. The ^{13}CO(1-0), ^{12}CO(1-0) and ^{12}CO(2-1) lines have upper energy levels E/k of 5.3 K, 5.5 K and 16.6 K, and critical densities of $2\times10^2\,\mathrm{cm}^{-3}$, $1\times10^3\,\mathrm{cm}^{-3}$ and $6.7\times10^3\,\mathrm{cm}^{-3}$ (for $T_{\mathrm{kin}} = 20\,\mathrm{K}$ and $\tau_{line} \simeq 1$), respec-

tively. We note that the critical density is a function of optical depth when line trapping effects are important (e.g., Scoville & Solomon 1974; Shirley 2015). In the case of ^{12}CO, the ^{12}CO(2-1)-to-^{12}CO(1-0) ratio would not only be sensitive to the temperature and density of the gas but also to the optical depth of ^{12}CO which may play a role in dictating where sub-thermal excitation happens (Peñaloza et al. 2017). On kpc-scales, our sample of galaxies span a range of CO(2-1)/CO(1-0) ratios between 0.3 and 2 and show a weak-to-moderate anti-correlation between $\mathfrak{R}$ and CO(2-1)/CO(1-0), indicating that $\mathfrak{R}$ decreases for increasing temperature/density/opacity (see Fig. 7 for model predictions). Both $\mathfrak{R}$ and CO(2-1)/CO(1-0), i.e. the y-axis and x-axis in Fig. 4a, are correlated via ^{12}CO(1-0). We investigate if the correlations are real or not by performing two Monte-Carlo tests that are detailed in Appendix B. Those tests indicate that the observed scatter in the line ratios is physical, it cannot be explained purely by noise. They also indicate that the correlation coefficients that we measure are robust and not driven by the correlated axes. Hence both the variations in the line ratios and the observed correlations are real.

PACS70/160 IR colour (Fig. 4b): All galaxies in our sample span a similar range of PACS70/PACS160 values ($0.2 - 0.8$). This IR colour can be used as a proxy for the dust temperature. We observe a weak-to-moderate anti-correlation of $\mathfrak{R}$ with PACS70/PACS160 for 5 galaxies: NGC 0628, NGC 4254, NGC 5055, NGC 5194, and NGC 6946. The high PACS70/PACS160 and low $\mathfrak{R}$ values are found in the centre of those galaxies, except for NGC 6946, where they are found in more diffuse regions of

the disc. Comparing ratio behaviors between Fig. 4a and Fig. 4b, temperature effects may be at play in those five galaxies, but it is probably not the dominant/unique condition affecting $\mathfrak{R}$.

SFR surface density (Fig. 4c): All galaxies in our sample span a similar range of Σ_{SFR} values, with NGC 0628 and NGC 3184 being a bit less active. We observe a weak correlation between $\mathfrak{R}$ and Σ_{SFR} for NGC 3184 and a moderate anti-correlation for NGC 4254 and NGC 5055. Those two galaxies have $\mathfrak{R}$ profiles steadily increasing with radius and also show an anti-correlation with the dust temperature. For NGC 3627, the behavior of $\mathfrak{R}$ with Σ_{SFR} is not immediately apparent from the radial profiles (Fig. 2), probably because the star-forming knots at the end of the bar and the centre have high Σ_{SFR} but different $\mathfrak{R}$ values. For the CARMA STING survey, Cao et al. (2017) also find no trend on global scales and moderately decreasing $\mathfrak{R}$ with increasing Σ_{SFR} for some galaxies, their galaxies probing the range $\Sigma_{SFR} \simeq 0.01 - 1.0 M_\odot\,yr^{-1}\,kpc^{-2}$.

$\Sigma_{SFR}/CO(1\text{-}0)$ *(Fig. 4d):* All galaxies in our sample span a similar range of $\Sigma_{SFR}/CO(1\text{-}0)$ values $(0.3 - 2\,Gyr^{-1})$, which we have normalized such that they have unit of star-formation efficiency (SFE_{mol}) under a constant, Galactic α_{CO} value. We find that $\mathfrak{R}$ is moderately anti-correlated with $\Sigma_{SFR}/CO(1\text{-}0)$ within all galaxies, i.e. that $\mathfrak{R}$ is lower at high efficiencies, though the two quantities are correlated by construction. As for the CO(2-1)/CO(1-0) intensity ratio, we test those correlations with Monte-Carlo simulations that are detailed in Appendix B. The test indicates that the scatter in the $\Sigma_{SFR}/CO(1\text{-}0)$ values is physical and cannot be purely explained by noise. The correlation coefficients are also robust and highest for NGC 5055 and NGC 6946. Previous works have suggested that variations in the star-formation efficiencies of massive galaxies could be linked to, e.g., a change in the relative fractions of diffuse and dense molecular gas (Saintonge et al. 2012; Shetty et al. 2014), or to enhanced CO excitation in galaxy centres (Leroy et al. 2013). Both effects have implications on the gas opacity and, though moderate, our trends indicate that the optical depth of CO, through $\mathfrak{R}$, could indeed account for some changes in star-formation efficiencies.

We also explored how $\mathfrak{R}$ correlates with UV/TIR (not shown). This ratio can be viewed as an indicator of the visible/obscured star-formation activity and, for a given geometry, of the ISM photodissociation/shielding ability. The EMPIRE galaxies span a wide range of values for the UV/TIR luminosity ratio. However, we find no clear correlation between $\mathfrak{R}$ and UV/TIR within galaxies.

Overall, most of the trends or lack of trends of $\mathfrak{R}$ with the physical parameters (Fig. 3 and Fig. 4) resemble the trends with galactocentric radius (Fig. 2). None of the parameters is revealing a strong positive or negative correlation, indicating that the kpc-scale resolution may be too coarse to isolate and identify the local effects affecting $\mathfrak{R}$.

3.5 Correlation between the X_{CO} factor and $\mathfrak{R}$

Since the physical quantities described above may also influence the conversion of $^{12}CO(1\text{-}0)$ intensity to molecular gas mass, we investigate empirically and with models how

Table 3. New average α_{CO} values using $^{12}CO(1\text{-}0)$ intensities and comparison to original values from Sandstrom et al. (2013). Standard deviations of values taken in the maps are indicated in dex in parenthesis. Helium is included.

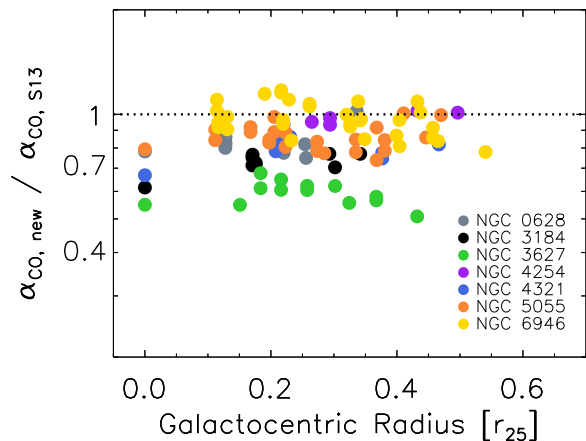|	$\alpha_{CO,new}$		$\alpha_{CO,new}/\alpha_{CO,S13}$	
NGC 0628	3.6	(0.2)	0.84	(0.04)
NGC 3184	4.3	(0.3)	0.73	(0.03)
NGC 3627	0.7	(0.2)	0.59	(0.03)
NGC 4254	4.3	(0.1)	0.98	(0.02)
NGC 4321	1.3	(0.3)	0.79	(0.04)
NGC 5055	3.1	(0.2)	0.86	(0.04)
NGC 6946	1.2	(0.2)	0.97	(0.05)
all galaxies	2.3	(0.4)	0.84	(0.08)

Figure 5. Pixel-by-pixel comparison of the α_{CO} values from Sandstrom et al. (2013) and those derived in this paper. There are no large trends within galaxies but the new α_{CO} values are slightly lower on average.

the variations in $\mathfrak{R}$ and in the X_{CO} factor, calibrated on the dust reference, are linked.

The X_{CO} factor can be determined indirectly from dust emission. Modeling of the dust emission provides a dust mass that is converted to a total gas mass with a dust-to-gas ratio and to a molecular mass by subtracting the mass of atomic gas. This molecular gas mass or surface density (denoted below Σ(mol,dust)) is then divided by the CO intensity to determine X_{CO} or α_{CO}. Leroy et al. (2011) first applied this by solving for the dust-to-gas ratio and α_{CO} simultaneously on spatially-resolved scales of a few kpc for the Local Group. That method was further employed in Sandstrom et al. (2013) for the HERACLES galaxies (including 8 out of the 9 galaxies of our sample) and is similarly applied to NGC 5194 in Leroy et al. (2017b) and Groves et al. (in prep.). In Sandstrom et al. (2013), α_{CO} is measured for hexagonal pixels of size 37.5 arcsec, using molecular surface densities from dust emission and HERACLES $^{12}CO(2\text{-}1)$ observations. They formally measure $\alpha_{CO(2-1)}$ that they express as $\alpha_{CO(1-0)}$ because $^{12}CO(1\text{-}0)$ is more commonly used. However, they adopt a fixed CO line ratio of 0.7. Here, with measurements of the $^{12}CO(2\text{-}1)/^{12}CO(1\text{-}0)$ ratio for each location, we update those α_{CO} values. As we
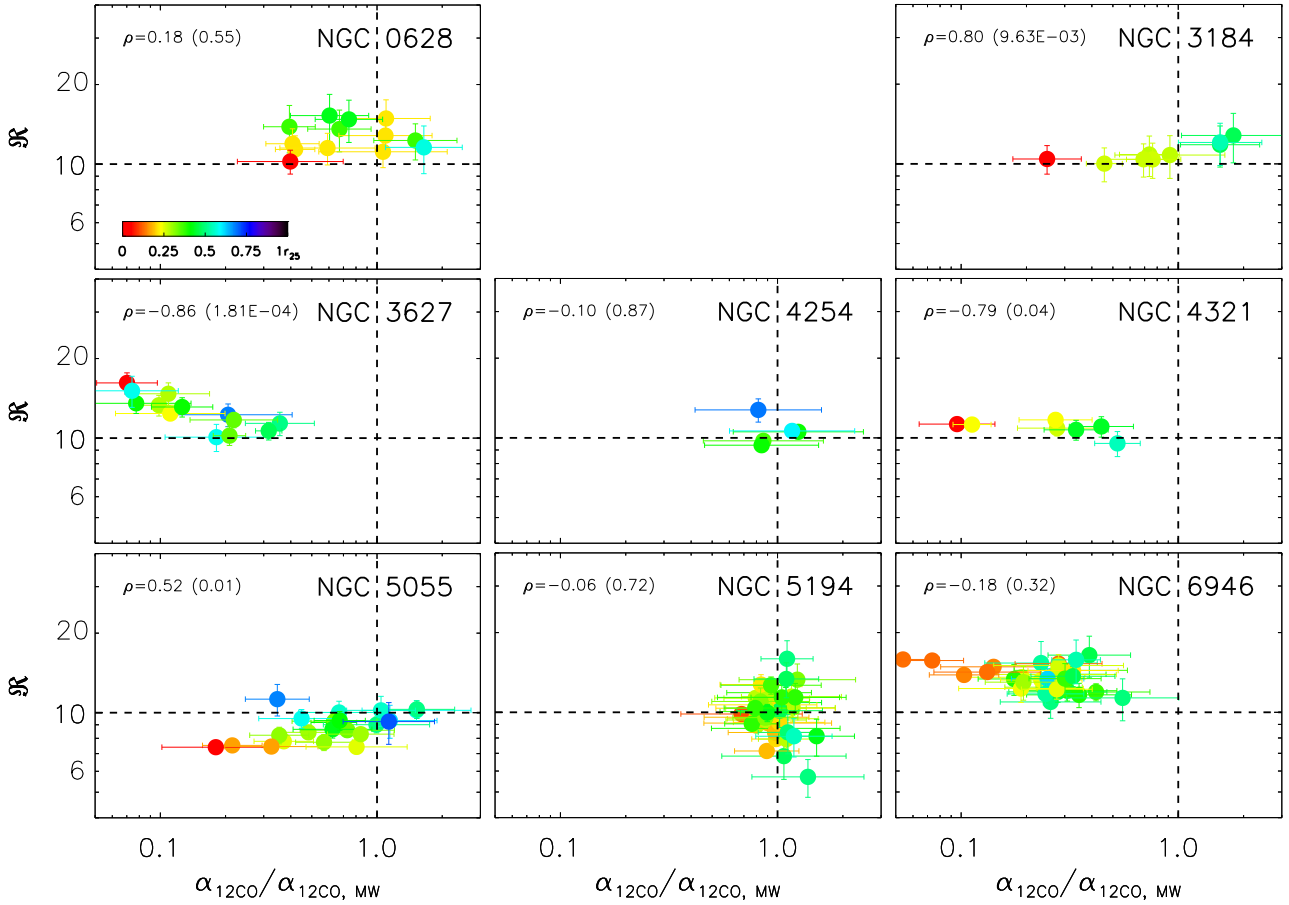
Figure 6. Correlation within galaxies of $\Re$ and the conversion factor α_{CO}, which is calibrated on dust emission. The trends are quite different from galaxy to galaxy. The colour-code corresponds to distance to the galaxy centre and it is the same for all panels. The dashed lines are shown to guide the eye. We also indicate the Spearman's rank correlation coefficients and their significance in parenthesis.

find $^{12}CO(2\text{-}1)/^{12}CO(1\text{-}0)$ ratios spanning a range of values between 0.3 and 2 on a kpc-scale in our sample of galaxies, we expect the α_{CO} values to change a bit. We calculate the average CO intensities and $\Re$ value in a circular aperture (roughly matched radius of 34.1 arcsec) centered on each of the pixels. The new conversion factor α_{CO} is equal to:

$$\alpha_{CO,new} = \Sigma(mol, dust) \, / \, I(^{12}CO(1-0)). \tag{1}$$

We show a pixel-to-pixel comparison of the old and new α_{CO} values in Figure 5, and we report averages of the new values, of ratios with the old values and dispersions in Table 3. The new α_{CO} values are about 15 per cent lower than the old values. There is a significant offset for NGC 3627 because its $^{12}CO(2\text{-}1)/^{12}CO(1\text{-}0)$ ratio is the lowest, with an average value of 0.5 as suggested by our new IRAM 30-m observations as opposed to the canonical value of 0.7 assumed by Sandstrom et al. (2013).

Figure 6 shows $\Re$ as a function of α_{CO}, normalized to the Milky Way value. $\Re$ and α_{CO} are positively correlated in NGC 5055 and NGC 3184, and more weakly in NGC 0628. $\Re$ and α_{CO} are anti-correlated in NGC 3627, NGC 4321, and rather weakly in NGC 6946, and the lowest α_{CO} values ($\leq 0.1\alpha_{CO,MW}$) are reached in those galaxies. In galaxy centres, one possible explanation for the low α_{CO} values observed is a change in the ^{12}CO optical depth (e.g., Sandstrom et al.

2013). Those optical depth effects seem to be at work in NGC 3627, NGC 6946, and to a lesser extent, NGC 4321.

3.6 Comparison to non-LTE models

To visualize how changes in physical conditions, specifically optical depth, density, and temperature, can affect $\Re$ quantitatively, we compare our observations to models from the non-LTE code RADEX (van der Tak et al. 2007). We note that those physical conditions, especially density and optical depth, could be correlated in real molecular clouds.

We use the grid of models built by Leroy et al. (2017a) to predict $\Re$, the $^{12}CO(2\text{-}1)/^{12}CO(1\text{-}0)$ intensity ratio, and X_{CO}. These models consider a distribution of volume densities (as an approximation for sub-beam density variations) and take into account sub-thermal excitation, but they assume fixed abundances and the spatial coexistence of ^{12}CO and ^{13}CO that fill the beam and are at a common kinetic temperature. In that sense, the models are representative of a single-phase medium, not of a multi-phase medium. Model predictions are scaled to our adopted ^{13}CO and ^{12}CO abundances (section 2.3.2). X_{CO} is computed as the inverse of the $^{12}CO(1\text{-}0)$ emissivity, ϵ_{12}, where $\epsilon_{12} = I_{12}/N_{12}$, I_{12} is the integrated intensity of $^{12}CO(1\text{-}0)$ and N_{12} is the column density of ^{12}CO. We vary the optical depth of the $^{12}CO(1\text{-}0)$
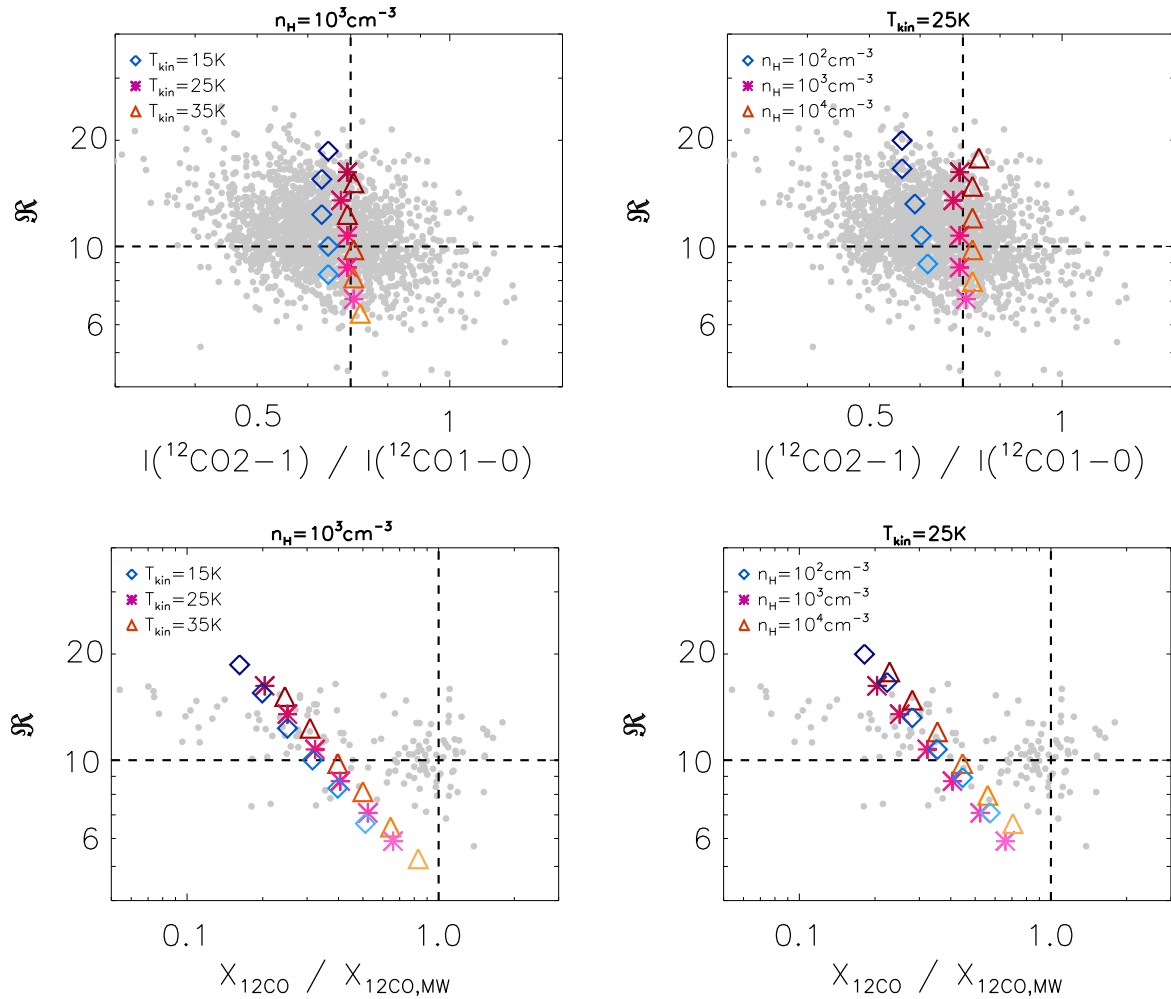
Figure 7. Correlation between $\Re$ and the ^{12}CO(2-1)/^{12}CO(1-0) ratio (top) and between $\Re$ and the X_{12CO} conversion factor (bottom) predicted by the RADEX grid of models from Leroy et al. (2017a). Observations are plotted in grey. The models show the expected trend, in LTE with filling factors of unity and fixed abundances, of X_{12CO} being inversely proportional to $\Re$ (see section 3.7). Optical depths τ_{12} are varied from 3 (dark-color symbols) to 10 (light-color symbols) in steps of 0.1 dex, while the ratio τ_{13}/τ_{12} is fixed to 0.03. Left panels: model predictions for kinetic temperatures of $T_{\rm kin} = 15$ K (blue diamonds), $T_{\rm kin} = 25$ K (purple asterisks), and $T_{\rm kin} = 35$ K (red triangles). The mean volume density is set to 10^3 cm^{-3}. Right panels: model predictions for mean volume densities of $n_{\rm H} = 10^2$ cm^{-3} (blue diamonds), $n_{\rm H} = 10^3$ cm^{-3} (purple asterisks), and $n_{\rm H} = 10^4$ cm^{-3} (red triangles). The kinetic temperature is set to 25 K.

line, τ_{12}, from 3 to 10 in steps of 0.1 dex. The ratio of the ^{13}CO(1-0) and ^{12}CO(1-0) line optical depths, τ_{13}/τ_{12}, is set to 0.03 and the effects of varying this value are discussed below. We assume a lognormal distribution of H$_2$ volume densities with a width $\sigma = 0.8$ dex. Several values of mean volume density ($n_{\rm H} = 10^2$, 10^3, 10^4 cm^{-3}) and temperature ($T_{\rm kin} = 15$, 25, 35 K) are tested. The predicted quantities that we investigate and the trends with density are somewhat sensitive to the selected width of the distribution, but not enough to change the results reported below.

Figure 7 shows predictions of $\Re$, ^{12}CO(2-1)/^{12}CO(1-0), and $X_{\rm CO}$. We discuss the effects of optical depth and density separately, but these could be correlated. As expected, the ^{12}CO(2-1)/^{12}CO(1-0) line ratio (top panels) increases for increasing temperature and density, and it is rather constant for increasing τ_{12} (same symbols, different shade). Concerning $X_{\rm CO}$ (bottom panels), $\Re$ decreases and $X_{\rm CO}$ increases with increasing τ_{12} because the ^{12}CO emissivity goes down.

$\Re$ is inversely proportional to $X_{\rm CO}$ (see also equation 6 in section 3.7), as long as τ_{13} remains small. The models predict an increase of $X_{\rm CO}$ or decrease of ^{12}CO emissivity – for a fixed τ – with increasing temperature. Increasing the temperature reduces the opacity per unit mass of ^{12}CO. But to keep τ constant, the increase in ^{12}CO intensity is not as large as the increase in gas column density because ^{12}CO is optically thick, hence its emissivity goes down. The models predict only mild variations of $\Re$ and $X_{\rm CO}$ with density: $\Re$ decreases most for a density of 10^3 cm^{-3} and $X_{\rm CO}$ increases linearly for the densities considered. This can be understood as the emissivity of ^{12}CO peaks at densities of 10^2 cm^{-3} (high $\Re$ and low $X_{\rm CO}$) while that of ^{13}CO peaks for densities 10^3 cm^{-3} (Leroy et al. 2017a).

Overall, we find that the models can only partially reproduce the observations. Density and temperature have a weaker impact on $\Re$ predictions than optical depth. The range of $\Re$ values found in the observations is covered

by the models, but the range of $^{12}CO(2\text{-}1)/^{12}CO(1\text{-}0)$ ratios and X_{CO} values is not. While one can imagine that a broader range of temperatures or densities (or a different opacity ratio) than tested could explain the range of observed $^{12}CO(2\text{-}1)/^{12}CO(1\text{-}0)$ ratios, the trends of $\mathfrak{R}$ with X_{CO} require additional modifications. Focusing on the isotopic abundance ratio (which is proportional to the optical depth ratio in LTE), here we discuss qualitatively which parameter space in the models is compatible with our observations:

(i) Galaxies with values in the disc of $\mathfrak{R} \simeq 10$ and $\alpha_{CO} \simeq \alpha_{CO,MW}$ (NGC 0628, NGC 3184, NGC 4254, NGC 5194), require the models in Fig. 7 to shift by a factor of 2 either to the right, which can be accomplished by decreasing the $^{12}CO/H_2$ abundance (keeping the isotopic ratio constant), or up, which can be accomplished by increasing the isotopic abundance ratio (keeping the $^{12}CO/H_2$ abundance constant).

(ii) The trend of higher $\mathfrak{R}$ values and lower α_{CO}, noted above for NGC 3627, NGC 6946, and to a lesser extent, NGC 4321, can naturally be explained with the models having low τ_{12} values ($\simeq 4$). In their centres, the lowest α_{CO} values still require the models to shift by a factor of $2-3$ either to the left, which can be accomplished by increasing the $^{12}CO/H_2$ abundance (keeping isotopic ratio constant), or down for very low τ_{12} values (^{12}CO becoming optically thin), which can be accomplished by lowering the isotopic abundance ratio (to $\simeq 20$).

(iii) The low $\mathfrak{R}$ and low α_{CO} values in the centre of NGC 5055 can be accounted for with the same modifications as for (ii), but for higher τ_{12} values.

In summary, for the discs of most of galaxies in our sample, the range of $\mathfrak{R}$ and X_{CO} values observed in can be explained by variations in optical depths (for a fixed optical depth ratio or isotopic abundance ratio). However some values, especially in galaxy centres, require a change by a factor of $2-3$ in the optical depth ratio (or isotopic abundance ratio), which seems reasonable. We should keep in mind that physical conditions may also be changing within the model grid (i.e. a multi-phase model would be more representative).

3.7 Optical depths and column densities

Since $^{13}CO(1\text{-}0)$ emission remains optically thin over larger parts of molecular clouds, it is often advocated as a more accurate tracer of the molecular gas mass than $^{12}CO(1\text{-}0)$ in the intermediate-density regime ($n_H \simeq 10^3$ cm^{-3}). In this section, we present the optical depth of the $^{13}CO(1\text{-}0)$ line (τ_{13}), ^{13}CO column densities (N_{13}), and H_2 column densities ($N(H_2)_{13CO}$) assuming local thermodynamic equilibrium (LTE). We compare the H_2 column densities to those obtained from $^{12}CO(1\text{-}0)$ emission. We opt for a simple framework as an alternative to the non-LTE models such as those presented in the previous section to have more flexibility on the choice of conditions/parameters and, in particular, explore the possibility of ^{12}CO and ^{13}CO having different filling factors. Ultimately, more lines and transitions would be needed for a complete, multi-phase modeling.

3.7.1 Framework

Given LTE, the equations of radiative transfer give the general expression for the observed brightness temperature of a line (T_{obs}):

$$T_{obs} = \eta_{bf}[J_\nu(T_{ex}) - J_\nu(T_{bg})](1 - \exp(-\tau)) \quad [K] \qquad (2)$$

where η_{bf} is the beam filling factor, J_ν is the line intensity given by the Planck function, T_{ex} is the excitation temperature, T_{bg} is the background temperature equal to 2.7 K, and τ is the optical depth of the line. To reduce this equation, we make the following assumptions for the $^{13}CO(1\text{-}0)$ and $^{12}CO(1\text{-}0)$ lines:
- $\tau_{12} > 1$ while $\tau_{13} \leq 1$,
- $\eta_{bf,12} = 1$ (^{12}CO fills the beam) while $\eta_{bf,13}$ is let free.

The optical depth τ_{13} and the column density N_{13} are given by:

$$\tau_{13} = -\ln\left(1 - \frac{1}{\eta_{bf,13}}\left[\frac{J_{\nu,12}(T_{ex,12}) - J_{\nu,12}(T_{bg})}{J_{\nu,13}(T_{ex,13}) - J_{\nu,13}(T_{bg})}\right] \times \frac{I_{13}}{I_{12}}\right) \qquad (3)$$

$$N_{13} = \frac{3.0 \times 10^{14}}{1 - \exp(-5.29/T_{ex,13})} \times \frac{\tau_{13}}{1 - \exp(-\tau_{13})} \times I_{13} \quad [cm^{-2}] \qquad (4)$$

where I is the integrated CO line intensity (in K km s^{-1}), obtained by integrating the line profiles which have similar shape and width for both CO lines. Equation 2 corresponds to equation (15.36) from Wilson et al. (2012). At the adopted T_{ex} values (≥ 20 K), we are in the Rayleigh-Jeans regime. The temperature term is an approximation of the partition function of CO with all energy levels populated in LTE. This simplification is valid for $T_{ex} \geq 8$ K. If τ_{13} is always small, N_{13} is an increasing function of T_{ex} because upper states get preferentially populated. We also assume that the continuum is weak (no IR pumping). We refer to Jiménez-Donaire et al. (2017b) for details of the calculations. In case the beam filling factor of ^{13}CO is lower than unity (hence lower than that of ^{12}CO), the quantities τ_{13} and N_{13} represent local values as opposed to beam-averaged values. To be able to compare H_2 column densities derived from $^{12}CO(1\text{-}0)$ and from $^{13}CO(1\text{-}0)$, we shall then consider beam-averaged quantities. The beam-averaged column density of H_2 can be deduced from $^{13}CO(1\text{-}0)$ with:

$$N(H_2)_{13CO} = N_{13} \times \left[\frac{H_2}{^{13}CO}\right] \times \frac{1}{\eta_{bf,13}} \quad [cm^{-2}]. \qquad (5)$$

From these formulae, for $\tau_{13} < 1$, the ^{12}CO-to-H_2 conversion factor will depend on $\mathfrak{R}$, which captures the optical depth of the ^{12}CO line. In this case:

$$X_{^{12}CO} = \left[\frac{H_2}{^{13}CO}\right] \times \frac{1}{\eta_{bf,13}} \times \frac{3.0 \times 10^{14}}{1 - \exp(-5.29/T_{ex,13})} \times \mathfrak{R}^{-1}$$
$$[cm^{-2}(K.km/s)^{-1}]. \qquad (6)$$

3.7.2 Results for τ_{13}, N_{13}, $N(H_2)$: simplest LTE case (Case 1)

To start with (Case 1), we assume thermalization of the lines and make the most simplifying assumptions, i.e. that both lines have the same excitation temperature, a beam filling factor equal to unity, abundances equal to the fiducial values, and X_{CO} equal to the Milky Way value. The assumed

parameters as well as the results for the ^{13}CO optical depths (τ_{13}) and column densities (N_{13} and $N(\text{H}_2)$) are reported in Table 4. We give average values of τ_{13} and N_{13} and their dispersion within the maps, for entire galaxies, their centres, and their discs.

Since our sample of galaxies display quite a narrow range of $\Re$ values, the average values for τ_{13} are very similar in all galaxies and around $0.07 - 0.11$. Those are beam-averaged values and correspond to $\tau_{12} \simeq 6$ (for an isotope abundance ratio of 60) and to a ^{12}CO effective critical density of $n_{\text{crit}} = n_{\text{crit,thin}}/\tau \simeq 2 \times 10^2 \, \text{cm}^{-3}$. For N_{13}, we find values in the range $0.4 - 2 \times 10^{15} \, \text{cm}^{-2}$ with a factor of two dispersion in the maps. Those correspond to ^{12}CO column densities of $0.2 - 1.2 \times 10^{17} \, \text{cm}^{-2}$ and are averages over large beams, not local quantities. The implied optically thin ^{13}CO-to-H$_2$ conversion factor is $8 \times 10^{20} \, \text{cm}^{-2} \, (\text{K km s}^{-1})^{-1}$.

We find that values of $N(\text{H}_2)_{13\text{CO}}$ are systematically lower by a factor of ~ 3 compared to $N(\text{H}_2)_{12\text{CO}}$ values. If our assumptions hold, either ^{13}CO traces poorly the total H$_2$ column densities, or ^{12}CO overpredicts the total H$_2$ column densities. Similar offsets in column densities were found by Meier et al. (2001); Meier & Turner (2004); Meier et al. (2008). Taking the ^{12}CO-based estimates as reference, we can speculate about mechanisms to increase the ^{13}CO-based estimate. To increase $N(\text{H}_2)_{13\text{CO}}$ by a factor of 3, we would need either an average excitation temperature of 60 K, an isotopic abundance ratio of 180, or a difference in beam filling factors of about 3. The maximum values allowed for each of those parameters and for each galaxy are reported in Table 4. We note that the beam filling factor can reflect variations in both abundances and emissivities of the lines but here we aim to separate the two effects and we consider that beam filling factors are dominated by emissivity variations. Although uncertainties associated to the adopted abundances are large, and temperatures in the galaxy centres may approach the required 60 K value (e.g., for NGC 6946, Walsh et al. 2002; Meier & Turner 2004), these requirements seem unlikely to be valid throughout the discs and in all discs of our sample. Moreover, if the temperature is indeed higher than the typical temperature of Galactic molecular clouds, then a Galactic conversion factor would also no longer apply for ^{12}CO. Hence, the discrepancies between H$_2$ column densities derived from ^{13}CO(1-0) and those derived from ^{12}CO(1-0) are most likely due to differences in beam filling factor of the two lines. Presumably, ^{12}CO(1-0) emission fills the beam and traces a more diffuse phase ($n < 10^3 \, \text{cm}^{-3}$) while ^{13}CO(1-0) emission is confined to a denser phase. In our sample of galaxies, the H$_2$ column densities can be explained by a filling factor fraction of diffuse versus dense gas that varies between 2.2 and 3.5, with a possible trend of higher fraction in galaxies with more clumpy star formation (e.g., NGC 0628, NGC 6946) and lower fraction in galaxies with strong spiral modes (e.g., NGC5055, NGC 5194).

3.7.3 Considerations on our assumptions

The discrepancy between the H$_2$ column densities derived from ^{13}CO(1-0) and those derived from ^{12}CO(1-0) may be due to oversimplifying assumptions, probably because, in our large beam size, we are probing clouds with a range of properties (densities, temperatures, opti-

cal depths; Szűcs et al. 2016; Leroy et al. 2017a). For example, abundance variations dependent on column density can change $N(\text{H}_2)_{13\text{CO}}$ by a factor of $2 - 3$ in Galactic molecular clouds (Goldsmith et al. 2008), though not sufficiently enough to reconcile LTE masses with the higher virial masses (Heyer et al. 2009). In the limit of co-existing ^{12}CO and ^{13}CO emission, and for a given set of physical conditions as chosen for *Case 1*, considering a sub-beam density distribution (section 3.6) would not be sufficient to reconcile column densities (models predict X_{CO} below the Milky-Way value). In numerical simulations of realistic molecular clouds, Szűcs et al. (2016) investigate how standard methods (^{13}CO and LTE, ^{12}CO and X_{CO}, the virial method) perform in recovering the true molecular mass/column density. They find that the ^{13}CO method is the worst predictor and systematically underpredicts the true mass by a factor of $2 - 3$ because of chemical and optical depth issues. Throughout our maps and with a beam size larger than the typical size of a molecular cloud, τ_{13} remains small, below 0.2, and the variations from beam to beam are not significant enough to change $N(\text{H}_2)_{13\text{CO}}$. It is possible that our $N(\text{H}_2)_{13\text{CO}}$ values are slightly underestimated because ^{13}CO is not completely optically thin and hides dense gas within the beam, although this explanation is unlikely. Indeed, in Galactic molecular clouds, τ_{13} can be locally enhanced on local, sub-parsec scales (e.g., Kramer et al. 1999, 2004; Jakob et al. 2007), but the impact on the global H$_2$ column densities derived is marginal (e.g., Wong et al. 2008). Our low values for τ_{13} are indicative of dense gas mixed with large amounts of diffuse gas within our (kpc-scale) beam.

^{12}CO(1-0) being optically thick leads to line trapping with the effect of lowering the critical density of the ^{12}CO line. ^{12}CO can emit strongly in low-density gas that makes up a large part of molecular clouds, and where ^{13}CO emission is weak because it is sub-thermally excited (e.g. Goldsmith et al. 2008; Leroy et al. 2017a). In that case, the fact that the bulk of the ^{12}CO and ^{13}CO emission does not trace the same gas can naturally explain the lower $N(\text{H}_2)_{13\text{CO}}$ values compared to the ^{12}CO-based estimates. To reasonable approximation, for optically thin emission the emissivity per molecule scales with the density for $n < n_{\text{crit}}$, and is constant for $n > n_{\text{crit}}$. The CO critical density in the optically thin case is $\sim 2,000 \, \text{cm}^{-3}$, so a factor of 3 correction in column densities would be expected if the volume density of the gas dominating the ^{13}CO emission were $\sim 700 \, \text{cm}^{-3}$. Conversely, one would only expect that the ^{13}CO would produce LTE-like levels of emission if the density were above $\sim 2,000 \, \text{cm}^{-3}$, which is clearly a large density for the bulk of molecular clouds. The ^{12}CO(1-0) emission is presumably more extended than the ^{13}CO(1-0) emission, as seen in resolved (pc-scales) studies (e.g., Pety et al. 2013). In the Milky Way, Roman-Duval et al. (2016) quantify the fraction of diffuse gas (gas detected in ^{12}CO(1-0) but not in ^{13}CO(1-0)) and dense gas (gas detected in both ^{12}CO(1-0) and ^{13}CO(1-0)). In terms of luminosity, they find that half of the gas is diffuse and half is dense in the outer disc, while in the inner disc, most of the gas ($\simeq 80$ per cent) is dense.

Non-LTE considerations, such as different excitation temperatures, abundances, and filling factors for the two lines (mimicking a two-phase model) are explored in the following *(Case 2)*.

Table 4. Results on optical depths and column densities.

Name	Assumed conditions					Derived quantities			Limits on conditions		
	$T_{ex,12}$ (K)	$T_{ex,13}$ (K)	$\frac{\eta_{bf,12}}{\eta_{bf,13}}$	$\frac{[^{12}\text{CO}]}{[^{13}\text{CO}]}$	$\frac{X_{\text{CO}}}{X_{\text{CO,MW}}}$	$\overline{\tau}_{13}$	$\overline{N}_{13}$ $(10^{15}\,\text{cm}^{-2})$	$\frac{N_{\text{H}_2,13\text{CO}}}{N_{\text{H}_2,12\text{CO}}}$	$T_{ex,13}^{l}$ (K)	$\frac{[^{12}\text{CO}]^{l}}{[^{13}\text{CO}]}$	$\frac{\eta_{bf,12}{}^{l}}{\eta_{bf,13}}$
Case 1: simple LTE conditions											
NGC 0628	20	20	1	60	1.0	0.07 (0.33 dex)	0.36 (0.38 dex)	0.29	80	210	3.4
NGC 2903	20	20	1	60	1.0	0.10 (0.10 dex)	1.96 (0.31 dex)	0.38	60	160	2.6
NGC 3184	20	20	1	60	1.0	0.09 (0.14 dex)	0.43 (0.23 dex)	0.36	65	170	2.8
NGC 3627	20	20	1	60	1.0	0.09 (0.18 dex)	1.65 (0.36 dex)	0.33	70	190	3.1
NGC 4254	20	20	1	60	1.0	0.09 (0.18 dex)	1.36 (0.43 dex)	0.38	60	160	2.6
NGC 4321	20	20	1	60	1.0	0.10 (0.09 dex)	1.27 (0.30 dex)	0.37	60	170	2.7
NGC 5055	20	20	1	60	1.0	0.11 (0.15 dex)	1.48 (0.35 dex)	0.46	50	130	2.2
NGC 5194	20	20	1	60	1.0	0.09 (0.30 dex)	1.01 (0.52 dex)	0.40	55	150	2.5
NGC 6946	20	20	1	60	1.0	0.07 (0.20 dex)	1.20 (0.41 dex)	0.29	80	210	3.5
Case 2: motivated choice of conditions											
NGC 0628 - centre	60	30	1	30	0.4	0.24 (0.09 dex)	1.40 (0.11 dex)	0.75	45	40	1.3
NGC 0628 - disc	30	20	2	60	0.7	0.26 (0.35 dex)	0.37 (0.39 dex)	0.86	25	70	2.3
NGC 2903 - centre	60	30	1	30	0.4*	0.20 (0.03 dex)	7.93 (0.08 dex)	0.65	50	50	1.5
NGC 2903 - disc	30	20	2	60	1.0*	0.37 (0.11 dex)	2.12 (0.28 dex)	0.88	25	70	2.3
NGC 3184 - centre	60	30	1	30	0.3	0.22 (0.03 dex)	1.61 (0.05 dex)	0.98	35	40	1.0
NGC 3184 - disc	30	20	2	60	0.9	0.35 (0.17 dex)	0.46 (0.22 dex)	0.93	25	70	2.1
NGC 3627 - centre	60	30	1	30	0.1	0.14 (0.08 dex)	4.96 (0.11 dex)	2.30	15	20	0.4
NGC 3627 - disc	30	20	2	60	0.2	0.31 (0.19 dex)	1.81 (0.37 dex)	2.07	15	20	0.4
NGC 4254 - centre	60	30	1	30	0.4*	0.29 (0.02 dex)	8.87 (0.04 dex)	0.93	35	40	1.1
NGC 4254 - disc	30	20	2	60	0.8	0.32 (0.20 dex)	1.40 (0.42 dex)	1.12	20	60	1.8
NGC 4321 - centre	60	30	1	30	0.1	0.21 (0.04 dex)	7.15 (0.16 dex)	2.47	15	20	0.4
NGC 4321 - disc	30	20	2	60	0.4	0.35 (0.11 dex)	1.16 (0.26 dex)	2.17	15	30	0.9
NGC 5055 - centre	60	30	1	30	0.2	0.34 (0.05 dex)	1.16 (0.09 dex)	2.31	15	20	0.4
NGC 5055 - disc	30	20	2	60	0.7	0.41 (0.17 dex)	1.60 (0.34 dex)	1.50	15	50	1.3
NGC 5194 - centre	60	30	1	30	0.4*	0.30 (0.06 dex)	11.4 (0.09 dex)	0.95	35	40	1.0
NGC 5194 - disc	30	20	2	60	1.0	0.33 (0.27 dex)	1.19 (0.44 dex)	0.93	25	70	2.2
NGC 6946 - centre	60	30	1	30	0.2*	0.15 (0.05 dex)	11.2 (0.22 dex)	0.87	40	40	1.2
NGC 6946 - disc	30	20	2	60	0.4	0.27 (0.20 dex)	1.08 (0.35 dex)	1.31	15	40	1.2

Notes. Column 1: galaxy name. Columns 2-3: assumed excitation temperatures of the ^{12}CO(1-0) and ^{13}CO(1-0) lines. Level population of the two levels of interest corresponding to the level population as predicted by LTE at the specific temperature. Column 4: assumed ratio of beam filling factors. Column 5: assumed isotope abundance ratio. Column 6: assumed value of the ^{12}CO(1-0)-to-H$_2$ conversion factor, normalized to the Milky Way value. The values are based on the results from Sandstrom et al. (2013) when available and otherwise (as indicated by the symbol *) motivated by Bolatto et al. (2013). Column 7: mean optical depth of the ^{13}CO(1-0) line and dispersion in the map in parenthesis. Column 8: column density of the ^{13}CO molecule and dispersion in the map in parenthesis. Column 9: ratio of H$_2$ column densities obtained from ^{13}CO(1-0) emission with the conditions given in columns 3-5 and from ^{12}CO(1-0) emission using the conversion factor given in column 6. Columns 10-11-12: maximum values allowed for the physical conditions such that column 9 equals to unity.

3.7.4 Results for τ_{13}, N_{13}, $N(\text{H}_2)$: motivated choice of conditions (Case 2)

In the second case, we allow for the lines to be non-thermalized and we adopt reasonable physical parameters for the centre and discs of our sample based on Galactic studies and on results from section 3.5. In the centres, the temperatures and filling factor of dense gas are assumed higher than in the discs, and the isotopic abundance is assumed lower. The assumed parameters and resulting quantities are listed in Table 4.

By allowing the excitation temperatures and the beam filling factors of the two CO lines to differ, the resulting τ_{13} values generally increase with respect to *Case 1*. τ_{13} is found around $0.14-0.34$ in the centres and around $0.26-0.41$ in the discs. N_{13} has similar values than in *Case 1* for the discs,

but larger values for the centres, around $1-11\times10^{15}\,\text{cm}^{-2}$, because of the higher temperatures used.

When we adopt more realistic conditions for the centres and discs of our sample, the values of $N(\text{H}_2)_{13\text{CO}}$ get closer to the values of $N(\text{H}_2)_{12\text{CO}}$ than in *Case 1*. The results are also very sensitive to the adopted X_{CO} factors. The X_{CO} values found by Sandstrom et al. (2013), based on dust emission, are generally lower than the standard Milky Way value. For the discs, the need for a higher filling factor of diffuse versus dense gas (by a factor of about 2) still persists in most galaxies. In the centres, the effect of a low X_{CO} value is somewhat compensated by adopting a lower isotope abundance ratio, without necessarily requiring a change in the beam filling factors. However, in NGC 3627, NGC 4321, and NGC 5055, the X_{CO} values are so low that this leads to

^{13}CO predicting twice more H_2 than ^{12}CO. In those galaxies, reconciling $N(H_2)_{13CO}$ with $N(H_2)_{12CO}$ requires either lower temperatures than assumed, or lower abundance ratios, or larger filling factors for ^{13}CO than for ^{12}CO. Both conditions on the temperatures and filling factors seem unrealistic and the need for changing abundances is in line with results from section 3.5. It is also possible that uncertainties on X_{CO} in those galaxies dominate here.

4 DISCUSSION

4.1 The $\mathfrak{R}$ ratio: origin of variations

The main trends of $\mathfrak{R}$ as a function of galactocentric radius that we find are: (1) a slight increase from centre to outer disc (by a factor of 2 at most); (2) offsets between galaxies (by a factor of 2 at most); (3) a high value in the centres of NGC 3627 and NGC 6946. Causes for $\mathfrak{R}$ variations are essentially linked to isotopic (or isotopolgue) abundances or gas physical conditions. They are discussed extensively for external galaxies in, e.g., Paglione et al. (2001); Tan et al. (2011); Danielson et al. (2013); Davis (2014) and briefly examined here:

■ *Changes in isotope abundance due to stellar nucleosynthesis* (e.g., Henkel & Mauersberger 1993; Casoli et al. 1992). After a recent burst, one expects the ^{12}C and ^{18}O abundances to be enhanced relative to the ^{13}C abundance (e.g., Meier et al. 2014; Sliwa et al. 2017b) and $\mathfrak{R}$ to increase, although the actual abundances are sensitive to the star-formation history and chemical effects within a galaxy. In the Milky Way, observations show an increase of the ^{12}C/^{13}C and ^{16}O/^{18}O abundance ratios with galactocentric radius (e.g., Milam et al. 2005) that can be reproduced by time-dependent models (e.g., Romano et al. 2017). A mild radial increase of the isotope abundance ratio (similar to or shallower than the gradient observed in the Milky Way) would naturally explain the steadily increasing $\mathfrak{R}$ profiles of some of the galaxies in our sample.

■ *Changes in abundance due to selective photo-dissociation* (e.g., Bally & Langer 1982; Visser et al. 2009). Since ^{13}CO is less abundant than ^{12}CO and their abundances are coupled, one expects ^{13}CO to be preferentially photo-dissociated under hard radiation fields. The effect is less clear for C^{18}O as it can be formed in a separate way (Bron et al. 2017). Simulating a suite of molecular clouds, Szűcs et al. (2014) showed that the effect of selective photo-dissociation on the ^{12}CO/^{13}CO abundance ratio is minimal. Jiménez-Donaire et al. (2017c) also argue that shielding from dust and H_2 dominates over self-shielding of CO molecules. Therefore, we do not consider selective photo-dissociation as a dominant effect.

■ *Changes in abundance due to chemical fractionation* (e.g., Liszt 2007). This process can enhance the abundance of ^{13}CO by a factor of $\sim$2-3 at low temperature and low optical depth in molecular clouds (Szűcs et al. 2014). It is believed to have a non-dominant effect on large (kpc) scales in the discs of galaxies (Paglione et al. 2001), though our C^{18}O(1-0) observations do not rule out fractionation as an important effect (Jiménez-Donaire et al. 2017c). The lowest $\mathfrak{R}$ ratios are found in the centres of a few galaxies and $\mathfrak{R}$ anti-correlates with dust temperature and Σ_{SFR} for those

galaxies, the inverse of what is expected from chemical fractionation. Hence we consider chemical fractionation as an unlikely explanation for the lowest $\mathfrak{R}$ values.

■ *Changes in physical conditions such as gas density, temperature, and opacity* (e.g., Pineda et al. 2008; Wong et al. 2008). Theoretically, we expect ^{13}CO(1-0) emission to trace denser and cooler gas than ^{12}CO(1-0). As explored in section 3.4, temperature/excitation may drive some of the lower $\mathfrak{R}$ values observed but it is not the only condition affecting $\mathfrak{R}$. The presence of diffuse emission or increased turbulence **(for example, due to a stellar bar)** would lower the optical depth of ^{12}CO(1-0) and boost its emission relative to ^{13}CO(1-0) (high $\mathfrak{R}$). Using several J transitions of ^{12}CO and ^{13}CO, Israel (2009a,b) model the centres of galaxies that have active nuclei with two ISM components, one hot and tenuous component with low optical depth, and one cooler and denser component. A different mixing of such two components (with different physical conditions or in different proportions) may explain the range of $\mathfrak{R}$ values observed in our sample of galaxies. The centre of NGC 3627 displays the largest ^{12}CO(1-0) line widths (noting that this includes resolution and inclination effects, and its strong stellar bar could add significant non-circular motions as well). In the centre of NGC 6946, Wu et al. (2017) also find larger velocity dispersions by analysing cloud-scale ^{12}CO(2-1) observations, although Meier & Turner (2004) do not find a correlation between line width and $\mathfrak{R}$.

We conclude that changes in the isotopic abundance due to nucleosynthesis or/and changes in the gas physical conditions, such as a different mixture of dense, cold gas and diffuse, warm gas that impacts on the mean opacity, could account for the trends with radius and offsets between galaxies. In the galaxy centres, **turbulence/bars** could account for the highest $\mathfrak{R}$ values that we observe, but their low α_{CO} values still argue for changes in isotopic abundances (section 3.5). To disentangle the effects of abundance and physical conditions on $\mathfrak{R}$, at least another ^{13}CO transition would be needed for a future, non-LTE modeling analysis.

4.2 ^{12}CO, ^{13}CO, and the X_{CO} conversion factor

In this section, we aim to understand under which circumstances ^{13}CO(1-0) can be used to improve estimates of the molecular gas mass.

4.2.1 $^{12}CO(1\text{-}0)$ and $^{13}CO(1\text{-}0)$ as tracers of star-formation and molecular gas mass

Galaxy centres are particularly interesting because they show some of the strongest variations in observations (including in $\mathfrak{R}$) and in physical properties in spiral galaxies. Several studies have found that the X_{CO} factor that converts ^{12}CO(1-0) intensity to molecular gas surface density is lower in the centres of galaxies (e.g., Oka et al. 2001; Zhu et al. 2009; Sandstrom et al. 2013). This could be due to factors such as an excess of ^{12}CO(1-0) emission from increased temperatures and large velocity dispersions lowering the optical depth of ^{12}CO (e.g., Bolatto et al. 2013). In our sample, high ^{12}CO(2-1)/^{12}CO(1-0) ratios, tracing higher temperatures/densities, are indeed observed in some galaxy centres (Leroy et al. 2009, 2013). The lowest X_{CO} factors are also
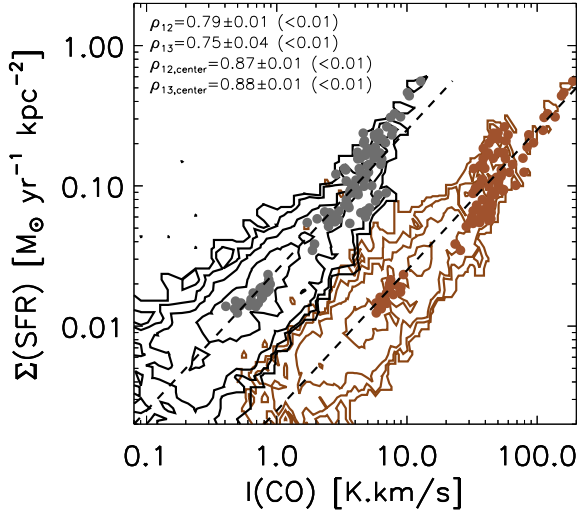
Figure 8. Correlation of Σ_{SFR} with both $^{13}CO(1-0)$ (black) and $^{12}CO(1-0)$ (brown) intensities of all EMPIRE galaxies. Density of data points are shown with contours and data points corresponding to galaxy centres are overplotted with filled circles. The dashed lines indicate a slope of 1. We also report the Spearman's rank correlation coefficients, their uncertainty, and their significance (in parenthesis), which are measured for a given CO line on all data points above a signal-to-noise ratio of 5 and measured on galaxy centres only.

found for galaxies with the highest $\mathfrak{R}$ (see section 3.5). In those cases, knowledge on both $^{12}CO(1-0)$ and $^{13}CO(1-0)$ emission can help reduce uncertainties on X_{CO} if the later is unknown. However, we do not find a systematic increase of $^{12}CO(1-0)$ emission relative to $^{13}CO(1-0)$ in the galaxy centres. This implies that, at kpc-scales in normal star-forming disc galaxies, the issues encountered when using $^{12}CO(1-0)$ as a tracer of the molecular gas mass are not systematically solved by using $^{13}CO(1-0)$.

Figure 8 shows the correlation between Σ_{SFR} and the $^{13}CO(1-0)$ and $^{12}CO(1-0)$ intensities of all EMPIRE galaxies. Density of data points are plotted as contours and data points corresponding to galaxy centres are overplotted (filled circles, centres are defined by a cut in CO intensity and radial distance, see section 3.2). The strengths of the correlations as well as the contour shapes are similar for both lines. The correlation between $^{12}CO(1-0)$ and Σ_{SFR} is marginally tighter than with $^{13}CO(1-0)$ when considering all data points and it is the same when considering centre points only. In the brightest regions ($\Sigma_{SFR} \geq 0.1\,M_\odot\,yr^{-1}\,kpc^{-2}$; corresponding to the centres of all galaxies except NGC 0628 and NGC 3184), the $^{13}CO(1-0)$ data points show slightly less scatter with Σ_{SFR} than $^{12}CO(1-0)$, and the star-formation efficiency from $^{13}CO(1-0)$ also has less scatter. In those bright regions, the distribution of $^{13}CO(1-0)$ data points tend to follow a superlinear relation with Σ_{SFR} while the distribution of $^{12}CO(1-0)$ data points appears to be bimodal with points (corresponding to NGC 6946) following a linear relation and points (corresponding to NGC 5194) following a super-linear relation. Hence ^{13}CO does not appear to be a more stable tracer of the SFR than ^{12}CO in our sample of disc galaxies, except at the high Σ_{SFR} end.

The analysis of H_2 column densities under the LTE as-

Table 5. The ^{13}CO-to-H_2 conversion factor in different regions of spirals.

	$X_{CO,13-total}$	$X_{CO,13-centre}$	$X_{CO,13-disc}$
average all	10.0 (0.29)	3.6 (0.25)	10.8 (0.29)
average nuc.[a]	4.9 (0.10)	2.2	5.3 (0.11)

Average values, in units of $10^{20}\,cm^{-2}\,(K\,km\,s^{-1})^{-1}$. The standard deviation is given in parenthesis and is in dex. The averages are measured as the mean of the logarithmic values of $X_{CO,13}$. (a) Galaxies with nuclear starbursts (NGC 2903, NGC 3627, NGC 4321, and NGC 6946).

sumption in section 3.7 has shown that $^{13}CO(1-0)$ systematically underpredicts masses of H_2, both in all pixels of our maps and if we consider integrated measurements. The behavior of the central pixels is obscured by the behavior of the more numerous disc pixels when looking at galaxies in their entirety. We have attributed the low H_2 column densities derived from $^{13}CO(1-0)$ in the discs to, mainly, the presence of diffuse gas that is traced by $^{12}CO(1-0)$ or dust emission but not by ^{13}CO. General methods to convert the dust and $^{12}CO(1-0)$ emission of galaxies to mass, however, are not calibrated on those diffuse phases and may overestimate the molecular gas mass. In turn, the presence of CO-dark gas could compensate somewhat for this overestimation (see Liszt et al. 2010; Liszt & Pety 2012). While ^{13}CO fails in retrieving the bulk molecular gas mass, its emission may vary less than ^{12}CO in the galaxy centres where the fraction of dense gas is larger and ^{13}CO traces better the intermediate-density regime ($\sim 1,000\,cm^{-3}$).

4.2.2 *The X_{CO} factor from $^{13}CO(1-0)$ emission*

We can derive an empirical X_{CO} factor from $^{13}CO(1-0)$ emission by dividing dust-based H_2 column densities (see section 3.7.3) by the $^{13}CO(1-0)$ intensity: $X_{CO,13} = N(H_2,dust)/I_{13}$ or $X_{CO,13} = X_{CO,12} \times \mathfrak{R}$. Figure 9 shows values of $X_{CO,13}$ (absolute and normalized to the average in each galaxy) as a function of distance to the centre for all galaxies. Averaged values in different parts of the galaxies are reported in Table 5. For entire galaxies, we find an average value of $X_{CO,13} = 1.0 \times 10^{21}\,cm^{-2}\,(K\,km\,s^{-1})^{-1}$ over our sample. If one were to consider a galactic conversion factor appropriate, then $X_{CO,13}$ can just be obtained by scaling X_{CO} with $\mathfrak{R}$, and the average $X_{CO,13}$ factor to use would be $2.2 \times 10^{21}\,cm^{-2}\,(K\,km\,s^{-1})^{-1}$.

As for $X_{CO,12}$ (Sandstrom et al. 2013), $X_{CO,13}$ has lower values in the galaxy centres, by a factor of ~ 3, and increases with distance. The scatter is large for absolute $X_{CO,13}$ values and reduces to less than a factor of 2 for $X_{CO,13}$ values normalized to each galaxy average. Such trends are also observed but less pronounced with Σ_{SFR} and the stellar surface density decreasing with increasing $X_{CO,13}$ because those quantities have higher values in galaxy centres. Sandstrom et al. (2013) found that the $^{12}CO(1-0)$-to-H_2 conversion factor, $X_{CO,12}$, varies more within the galaxies dominated by a central starburst: it is about one order of magnitude lower than the Galactic value in the centres and three times lower on average. Such low con-
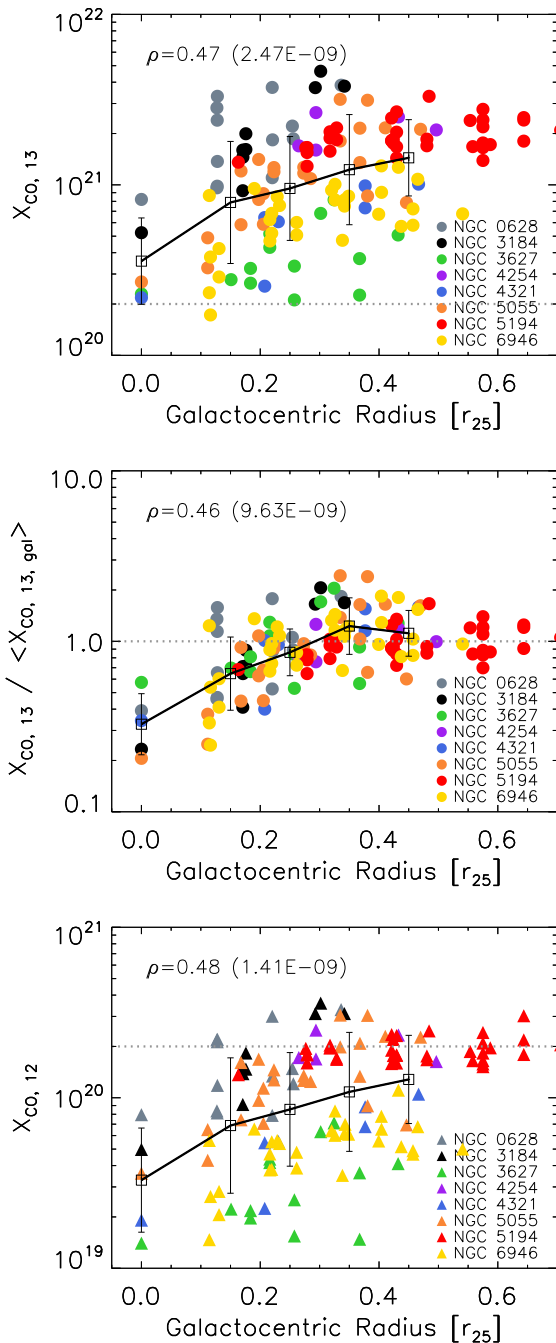
Figure 9. Top panel: Empirical X_{CO} factor showing values lower than average in the galaxy centres and increasing with distance from the centre. $X_{CO,13}$ is derived from dust-based H_2 column densities and $^{13}CO(1\text{-}0)$ emission, in units of $cm^{-2}\,(K\,km\,s^{-1})^{-1}$. The black open squares and curve show the mean values and dispersion of all data points within bins of width $0.1\,r_{25}$. The horizontal dotted line indicates the typical value of the ^{12}CO-to-H_2 conversion factor in the Milky Way. We also report Spearman's rank correlation coefficients and their significance in parenthesis. Middle panel: Same as above, normalized to the mean $X_{CO,13}$ value in each galaxy. Bottom panel: Same as the top panel for $^{12}CO(1\text{-}0)$ emission.

version factors can be found for extreme starbursts like LIRGs (Downes & Solomon 1998; Kamenetzky et al. 2014; Sliwa et al. 2017a). The galaxies dominated by a central starburst in Sandstrom et al. (2013) that are overlapping with our EMPIRE sample are NGC 3627, NGC 4321, and NGC 6946 (bottom panel of Figure 9). Those galaxies have higher $\Re$ values in their centres and on average. The top panel of Figure 9 shows that they have lower $X_{CO,13}$ than the other galaxies on average, and slightly less variation from centre to outer disc than with $^{12}CO(1\text{-}0)$ because of their declining $\Re$ profiles. Within galaxies, $X_{CO,13}$ and $X_{CO,12}$ show a similar dispersion of ~0.2 dex, but there are still large variations from galaxy to galaxy. Taking all galaxies together, the dispersion per radial bin is about 0.30 dex for $X_{CO,13}$ and 0.35 dex for $X_{CO,12}$.

Overall, our results suggest that the observed changes in $X_{CO,12}$ cannot be explained purely by ^{12}CO optical depth effects. In that case we would expect $X_{CO,13}$ to stay approximately constant, while $X_{CO,12}$ changes. In contrast, our observations favor variations in $X_{CO,13}$ as well, with lower values in the centres. This suggests that some combination of varying parameters (abundance, optical depth, etc.) is also affecting $X_{CO,13}$. We note that these conclusions are all tied to H_2 column estimates from the dust-based method, so they are subject to the same systematic uncertainties inherent in that technique.

5   CONCLUSIONS

We present new observations of the $^{13}CO(1\text{-}0)$ emission from the EMPIRE survey (Bigiel et al. 2016; Jiménez-Donaire et al. 2017a) and of the $^{12}CO(1\text{-}0)$ emission from follow-up programs obtained with the IRAM 30-m in 9 nearby spiral galaxies (NGC 0628, NGC 2903, NGC 3184, NGC 4254, NGC 4321, NGC 5055, NGC 6946; and NGC 5194 from PAWS, Pety et al. 2013). $^{13}CO(1\text{-}0)$ is detected at high signal-to-noise across the entire molecular disc in those galaxies. We summarize our results as follows:

- The integrated intensity of $^{13}CO(1\text{-}0)$ is on average 11 times fainter than that of $^{12}CO(1\text{-}0)$. The $^{12}CO(1\text{-}0)$-to-$^{13}CO(1\text{-}0)$ intensity ratio ($\Re$) does not vary significantly within or amongst galaxies in our sample (at a resolution of ~1.5 kpc), by a factor of ~2 at most, and the spread in values is largest in the galaxy centres. On those spatial scales, the $^{12}CO(2\text{-}1)$-to-$^{12}CO(1\text{-}0)$ ratio varies between 0.3 and 2.

- We correlate $\Re$ with several physical quantities on global and resolved scales. We find no strong trend on global scales. On resolved scales, $\Re$ anti-correlates weakly to moderately with the $^{12}CO(2\text{-}1)/^{12}CO(1\text{-}0)$ ratio, the IR colour, Σ_{SFR}, and the SFE ($\Sigma_{SFR}/\Sigma_{H_2}$). Anti-correlations are more visible for galaxies with lowest $\Re$ values in their centres (NGC 4254, NGC 5055, NGC 5194), which we interpret as a local temperature/excitation effect. However, other conditions such as density/optical depths must be at play to explain all $\Re$ behaviors.

- We find that galaxies with starburst-dominated nuclei (which are also barred galaxies) have higher $\Re$ values in their centres than the other galaxies in our sample. In those galaxies, the anti-correlation of $\Re$ with the α_{CO} conversion factor from dust is compatible with optical depth effects. Changes

in the isotope abundance ratio from stellar nucleosynthesis due to the recent central bursts are also possible.

- Assuming LTE and fixed abundances, we compute optical depths and column densities for the $^{13}CO(1-0)$ line. Beam-averaged optical depths are on the order of 0.1. We find that the H_2 column densities derived from $^{13}CO(1-0)$ are systematically lower by a factor of $2-3$ than those derived from $^{12}CO(1-0)$. Those discrepancies can be mainly explained by non-LTE effects (significant diffuse phase in the discs where ^{13}CO is sub-thermally excited) or departure of abundances from nominal galactic values.

- Assuming H_2 column densities from dust emission, we calculate an empirical $^{13}CO(1-0)$-to-H_2 conversion factor. The average value found in our sample is $1.0 \times 10^{21} \, \mathrm{cm^{-2} \, (K \, km \, s^{-1})^{-1}}$. It increases from galaxy centre to outer disc with similar scatter (~ 0.3 dex) than the $^{12}CO(1-0)$-to-H_2 conversion factor (based on $^{12}CO(2-1)$ data; Sandstrom et al. 2013). Except in the centres, ^{13}CO does not appear as a more stable tracer of the molecular gas mass or star-formation rate than $^{12}CO(1-0)$ in normal star-forming disc galaxies.

Despite being optically thin, the use of $^{13}CO(1-0)$ emission as a tracer of total mass seems to be limited in normal star-forming disc galaxies, due to the presence of a significant diffuse phase and variations in physical conditions of the gas and abundances. To constrain those, systematic observations of at least one more ^{13}CO transitions will be an important next step.

ACKNOWLEDGEMENTS

References

Aalto S., Booth R. S., Black J. H., Johansson L. E. B., 1995, A&A, 300, 369

Alatalo K., et al., 2015, MNRAS, 450, 3874

Aniano G., Draine B. T., Gordon K. D., Sandstrom K., 2011, PASP, 123, 1218

Arimoto N., Sofue Y., Tsujimoto T., 1996, PASJ, 48, 275

Bally J., Langer W. D., 1982, ApJ, 255, 143

Bendo G. J., Galliano F., Madden S. C., 2012, MNRAS, 423, 197

Bigiel F., et al., 2016, ApJ, 822, L26

Bolatto A. D., Wolfire M., Leroy A. K., 2013, ARA&A, 51, 207

Bron E., et al., 2017, preprint, (arXiv:1710.07288)

Cao Y., Wong T., Xue R., Bolatto A. D., Blitz L., Vogel S. N., Leroy A. K., Rosolowsky E., 2017, preprint, (arXiv:1709.00066)

Casoli F., Dupraz C., Combes F., 1992, A&A, 264, 55

Chomiuk L., Povich M. S., 2011, AJ, 142, 197

Cormier D., et al., 2014, A&A, 564, A121

Dale D. A., et al., 2009, ApJ, 693, 1821

Dame T. M., Hartmann D., Thaddeus P., 2001, ApJ, 547, 792

Danielson A. L. R., et al., 2013, MNRAS, 436, 2793

Davis T. A., 2014, MNRAS, 445, 2378

Dickman R. L., 1978, ApJS, 37, 407

Downes D., Solomon P. M., 1998, ApJ, 507, 615

Encrenaz P. J., Stark A. A., Combes F., Wilson R. W., 1979, A&A, 78, L1

Fukui Y., Kawamura A., 2010, ARA&A, 48, 547

Galametz M., et al., 2013, MNRAS, 431, 1956

Gallagher M., et al., 2017, Dense gas, dynamical equilibrium pressure, and star formation in four nearby star-forming galaxies, submitted

Garcia-Burillo S., Guelin M., Cernicharo J., 1993, A&A, 274, 123

Goldsmith P. F., Heyer M., Narayanan G., Snell R., Li D., Brunt C., 2008, ApJ, 680, 428

Henkel C., Mauersberger R., 1993, A&A, 274, 730

Henkel C., et al., 2014, A&A, 565, A3

Heyer M., Dame T. M., 2015, ARA&A, 53, 583

Heyer M., Krawczyk C., Duval J., Jackson J. M., 2009, ApJ, 699, 1092

Ho L. C., Filippenko A. V., Sargent W. L. W., 1997, ApJ, 487, 591

Israel F. P., 2009a, A&A, 493, 525

Israel F. P., 2009b, A&A, 506, 689

Jakob H., Kramer C., Simon R., Schneider N., Ossenkopf V., Bontemps S., Graf U. U., Stutzki J., 2007, A&A, 461, 999

Jiménez-Donaire M. J., et al., 2017a, EMPIRE dense gas relations, in prep.

Jiménez-Donaire M. J., et al., 2017b, MNRAS, 466, 49

Jiménez-Donaire M. J., et al., 2017c, ApJ, 836, L29

Kamenetzky J., Rangwala N., Glenn J., Maloney P. R., Conley A., 2014, ApJ, 795, 174

Kennicutt R. C., Evans N. J., 2012, ARA&A, 50, 531

Kennicutt Jr. R. C., et al., 2003, PASP, 115, 928

Kennicutt R. C., et al., 2011, PASP, 123, 1347

Kramer C., Alves J., Lada C. J., Lada E. A., Sievers A., Ungerechts H., Walmsley C. M., 1999, A&A, 342, 257

Kramer C., Jakob H., Mookerjea B., Schneider N., Brüll M., Stutzki J., 2004, A&A, 424, 887

Kreckel K., Groves B., Bigiel F., Blanc G. A., Kruijssen J. M. D., Hughes A., Schruba A., Schinnerer E., 2017, ApJ, 834, 174

Krips M., Crocker A. F., Bureau M., Combes F., Young L. M., 2010, MNRAS, 407, 2261

Langer W. D., Penzias A. A., 1990, ApJ, 357, 477

Leroy A. K., et al., 2009, AJ, 137, 4670

Leroy A. K., et al., 2011, ApJ, 737, 12

Leroy A. K., et al., 2013, AJ, 146, 19

Leroy A. K., et al., 2017a, ApJ, 835, 217

Leroy A. K., et al., 2017b, ApJ, 846, 71

Li F.-C., Wu Y.-W., Xu Y., 2015, Research in Astronomy and Astrophysics, 15, 785

Liszt H. S., 2007, A&A, 476, 291

Liszt H. S., Pety J., 2012, A&A, 541, A58

Liszt H. S., Pety J., Lucas R., 2010, A&A, 518, A45

Martín S., Aladro R., Martín-Pintado J., Mauersberger R., 2010, A&A, 522, A62

Meier D. S., Turner J. L., 2004, AJ, 127, 2069

Meier D. S., Turner J. L., Crosthwaite L. P., Beck S. C., 2001, AJ, 121, 740

Meier D. S., Turner J. L., Hurt R. L., 2008, ApJ, 675, 281

Meier D. S., Turner J. L., Beck S. C., 2014, ApJ, 795, 107

Milam S. N., Savage C., Brewster M. A., Ziurys L. M., Wyckoff S., 2005, ApJ, 634, 1126

Muraoka K., et al., 2016, PASJ, 68, 89

Murphy E. J., et al., 2011, ApJ, 737, 67

Narayanan D., Krumholz M., Ostriker E. C., Hernquist L., 2011, MNRAS, 418, 664

Oka T., Hasegawa T., Sato F., Tsuboi M., Miyazaki A., Sugimoto M., 2001, ApJ, 562, 348

Paglione T. A. D., et al., 2001, ApJS, 135, 183

Papadopoulos P. P., van der Werf P., Xilouris E., Isaak K. G., Gao Y., 2012, ApJ, 751, 10

Peñaloza C. H., Clark P. C., Glover S. C. O., Shetty R., Klessen R. S., 2017, MNRAS, 465, 2277

Pety J., et al., 2013, ApJ, 779, 43

Pineda J. E., Caselli P., Goodman A. A., 2008, ApJ, 679, 481

Roman-Duval J., Heyer M., Brunt C. M., Clark P., Klessen R., Shetty R., 2016, ApJ, 818, 144

Romano D., Matteucci F., Zhang Z.-Y., Papadopoulos P. P., Ivison R. J., 2017, MNRAS, 470, 401

Saintonge A., et al., 2012, ApJ, 758, 73

Sakamoto S., Handa T., Sofue Y., Honma M., Sorai K., 1997, ApJ, 475, 134

Sandstrom K. M., et al., 2013, ApJ, 777, 5

Schinnerer E., et al., 2013, ApJ, 779, 42

Scoville N. Z., Solomon P. M., 1974, ApJ, 187, L67

Sheffer Y., Rogers M., Federman S. R., Abel N. P., Gredel R., Lambert D. L., Shaw G., 2008, ApJ, 687, 1075

Shetty R., Glover S. C., Dullemond C. P., Ostriker E. C., Harris A. I., Klessen R. S., 2011, MNRAS, 415, 3253

Shetty R., Clark P. C., Klessen R. S., 2014, MNRAS, 442, 2208

Shirley Y. L., 2015, PASP, 127, 299

Sliwa K., Wilson C. D., Matsushita S., Peck A. B., Petitpas G. R., Saito T., Yun M., 2017a, ApJ, 840, 8

Sliwa K., Wilson C. D., Aalto S., Privon G. C., 2017b, ApJ, 840, L11

Solomon P. M., Sage L. J., 1988, ApJ, 334, 613

Sternberg A., Le Petit F., Roueff E., Le Bourlot J., 2014, ApJ, 790, 10

Szűcs L., Glover S. C. O., Klessen R. S., 2014, MNRAS, 445, 4055

Szűcs L., Glover S. C. O., Klessen R. S., 2016, MNRAS, 460, 82

Tan Q.-H., Gao Y., Zhang Z.-Y., Xia X.-Y., 2011, Research in Astronomy and Astrophysics, 11, 787

Tielens A. G. G. M., Hollenbach D., 1985, ApJ, 291, 722

Tosaki T., Hasegawa T., Shioya Y., Kuno N., Matsushita S., 2002, PASJ, 54, 209

Vila-Vilaro B., Cepa J., Zabludoff A., 2015, ApJS, 218, 28

Visser R., van Dishoeck E. F., Black J. H., 2009, A&A, 503, 323

Walsh W., Beck R., Thuma G., Weiss A., Wielebinski R., Dumke M., 2002, A&A, 388, 7

Wang M., Chin Y.-N., Henkel C., Whiteoak J. B., Cunningham M., 2009, ApJ, 690, 580

Wilson T. L., Rood R., 1994, ARA&A, 32, 191

Wilson C. D., Walker C. E., Thornley M. D., 1997, ApJ, 483, 210

Wilson T. L., Rohlfs K., Huttemeister S., 2012, Tools of Radio Astronomy, 5th edition

Wolfire M. G., Hollenbach D., McKee C. F., 2010, ApJ, 716, 1191

Wong T., et al., 2008, MNRAS, 386, 1069

Wu Y.-L., Sakamoto K., Pan H.-A., 2017, ApJ, 839, 6

Young J. S., Sanders D. B., 1986, ApJ, 302, 680

Zhu M., Papadopoulos P. P., Xilouris E. M., Kuno N., Lisenfeld U., 2009, ApJ, 706, 941

de Vaucouleurs G., Pence W. D., 1978, AJ, 83, 1163

van Dishoeck E. F., Black J. H., 1988, ApJ, 334, 771

van Dishoeck E. F., Glassgold A. E., Guelin M., Jaffe D. T., Neufeld D. A., Tielens A. G. G. M., Walmsley C. M., 1992, in Singh P. D., ed., IAU Symposium Vol. 150, Astrochemistry of Cosmic Phenomena. p. 285

van der Tak F. F. S., Black J. H., Schöier F. L., Jansen D. J., van Dishoeck E. F., 2007, A&A, 468, 627

APPENDIX A: EMPIRE ^{13}CO(1-0) OBSERVATIONS AND RADIAL PROFILES

This Appendix presents an atlas of the dust continuum at $70\,\mu$m, ^{13}CO(1-0) emission, and $\Re$ in the EMPIRE galaxies, as well as radial profiles and stacked spectra of CO lines for each galaxy.

APPENDIX B: MONTE-CARLO TEST OF RATIO VARIATIONS

We perform two Monte-Carlo tests regarding the ratios CO(2-1)/CO(1-0), Σ(SFR)/CO(1-0), and $1/\Re$.

CO(2-1)/CO(1-0) and $1/\Re$: For the first test, we aim to understand whether there are real physical variations in the line ratios or whether the scatter in line ratio values can be explained by noise only. The distribution of lines ratios using noisy data is non-Gaussian even if the noise on the line measurements is Gaussian. Here we are not interested in the exact shape of the distribution of the line ratios but rather whether the observed range could be driven by the uncertainties on the line measurements. To this end we compare the line ratio distribution with Monte-Carlo simulations as follows. We consider the observed ^{12}CO(1-0) intensities as true values and generate new ^{13}CO(1-0) and ^{12}CO(2-1) intensities considering fixed line ratios with ^{12}CO(1-0) and adding noise based on the observed uncertainties of each measurement. The value of the fixed line ratio is set to the median of the observed ratios, though this value does not really matter for this experiment. We iterate this process 1 000 times, and, for each iteration, we calculate the standard deviation of the simulated line ratios. For both $\Re$ and CO(2-1)/CO(1-0), we find that the peak of the distribution of those standard deviations is systematically lower by a factor of ∼2 compared to the standard deviation of the observed line ratios. The peak is closer to the observed value only for $\Re$ in NGC 3184. Hence we conclude that the scatter in the observed $\Re$ and CO(2-1)/CO(1-0) ratios is largely physical. For the second test, we aim to verify the robustness of the correlation coefficients measured in Fig. 4a. For this, we generate new ^{13}CO(1-0), ^{12}CO(1-0), and ^{12}CO(2-1) intensities by taking the observed intensities and adding noise based on the observed uncertainties of each measurement. We also iterate the process 1 000 times. We find that the peak of the distribution of standard deviations is slightly larger than the standard deviation of the observed ratios because of the noise added by the simulations. For each iteration, we measure the correlation coefficient and slope between $\Re$ and CO(2-1)/CO(1-0). We find that the distribution of the correlation coefficients is well peaked around the coefficient measured on the observations. This indicates that the correlations persist after adding noise. The distribution of the slopes generally peaks around 0.5 and it is
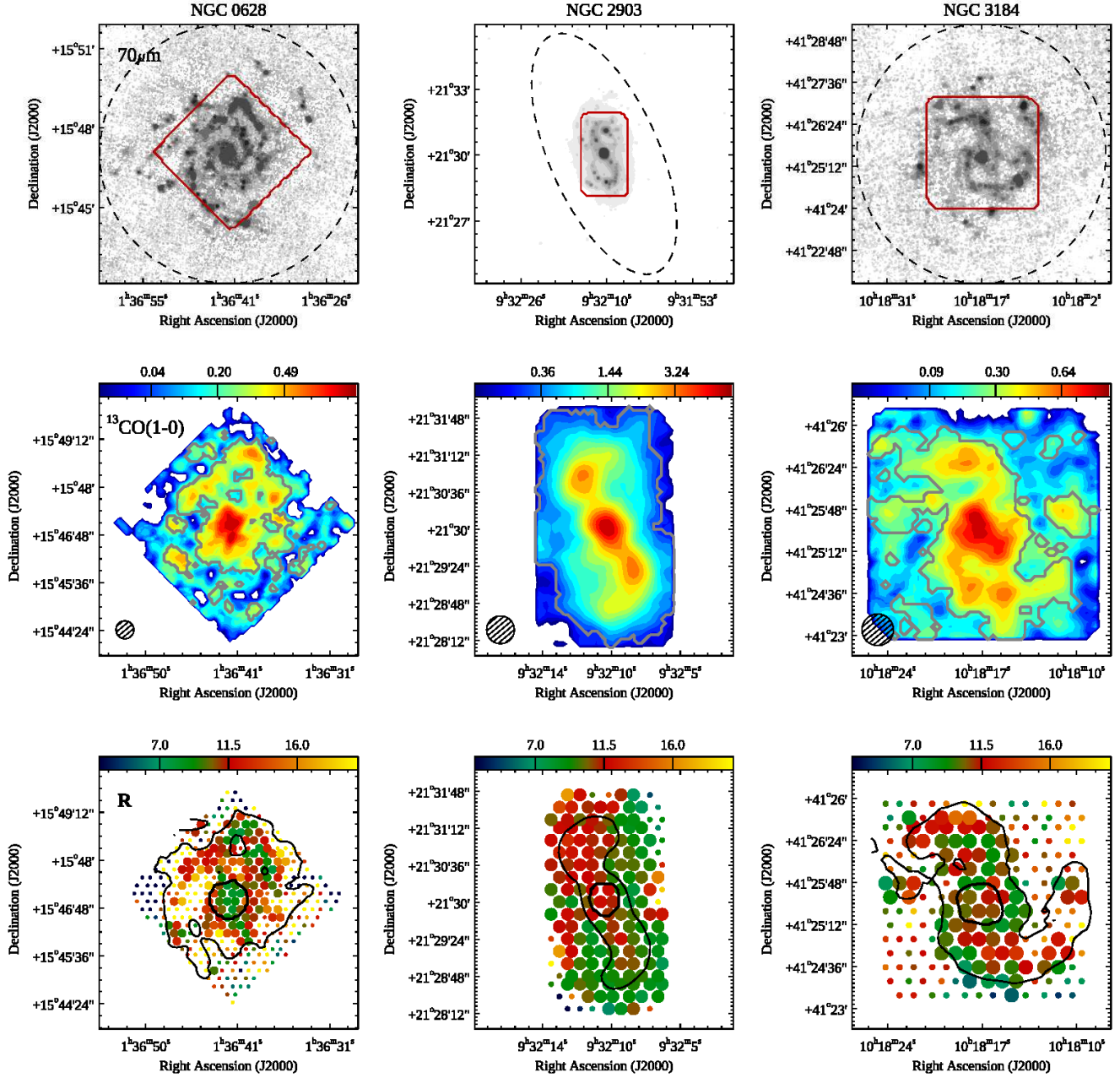
Figure A1. Atlas of infrared dust continuum, ^{13}CO(1-0) integrated intensity, and ^{12}CO(1-0)-to^{13}CO(1-0) ratio ($\mathcal{R}$) for the EMPIRE galaxies. <u>Top panels:</u> *Herschel* 70 μm map (*Spitzer* 24 μm map in the case of NGC 2903), in square root scale. The dashed ellipse shows the r_{25} radius and the red contours show the IRAM coverage. <u>Middle panels:</u> ^{13}CO(1-0) integrated intensity map, in square root scale. The colourbar is in units of K km s^{-1}. The beam size of 27 arcsec is indicated on the bottom left corner. Contours at 5σ are shown in grey. <u>Bottom panels:</u> Map of $\mathcal{R}$ where we draw a filled circle for each sampling point. Smaller circles correspond to sampling points with signal-to-noise ratio of $\mathcal{R}$ below 5. Black contours delineate the center and arm regions that are defined by eye on the ^{12}CO(1-0) intensity maps and used for stacking (see section 3.2).
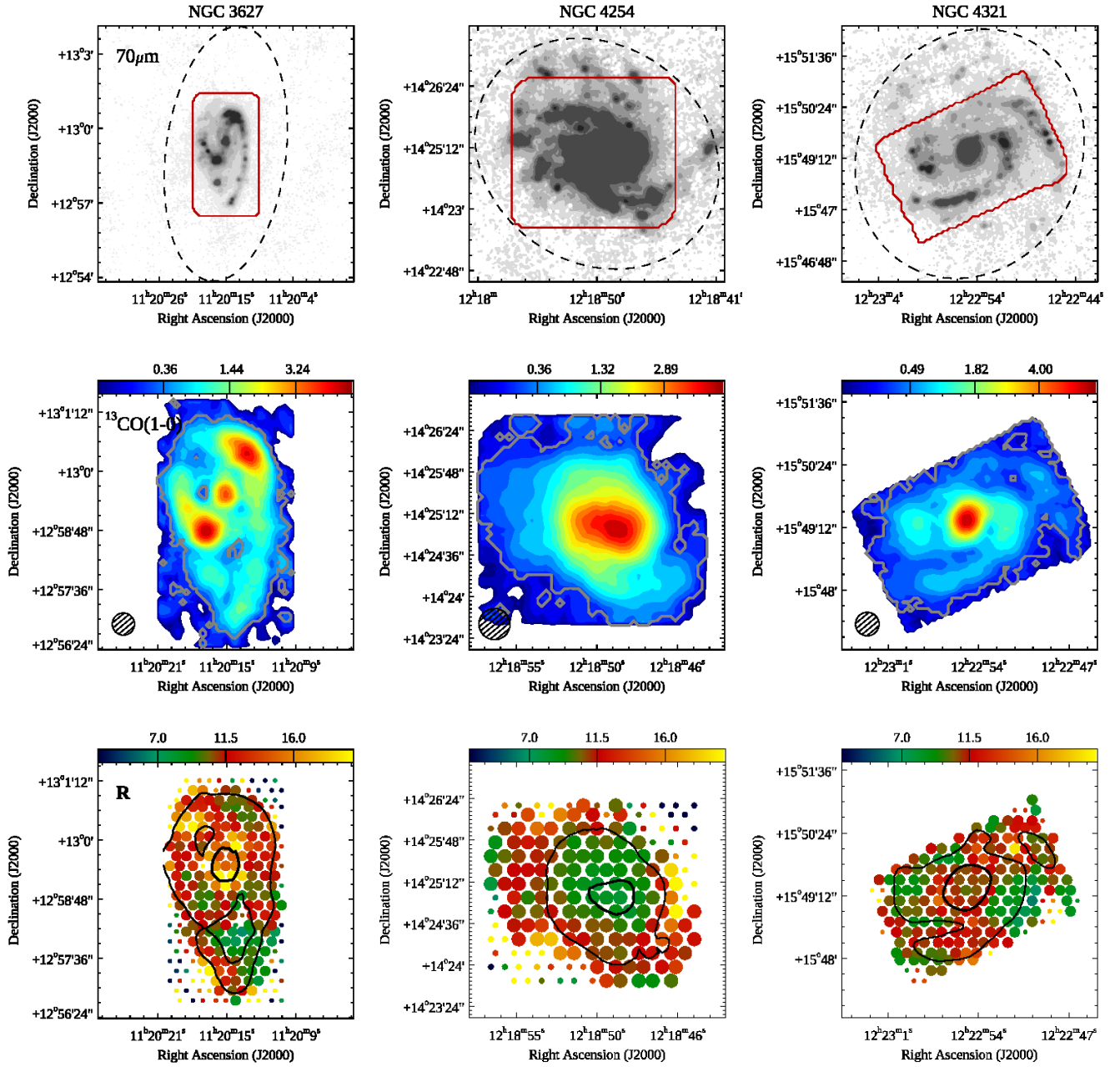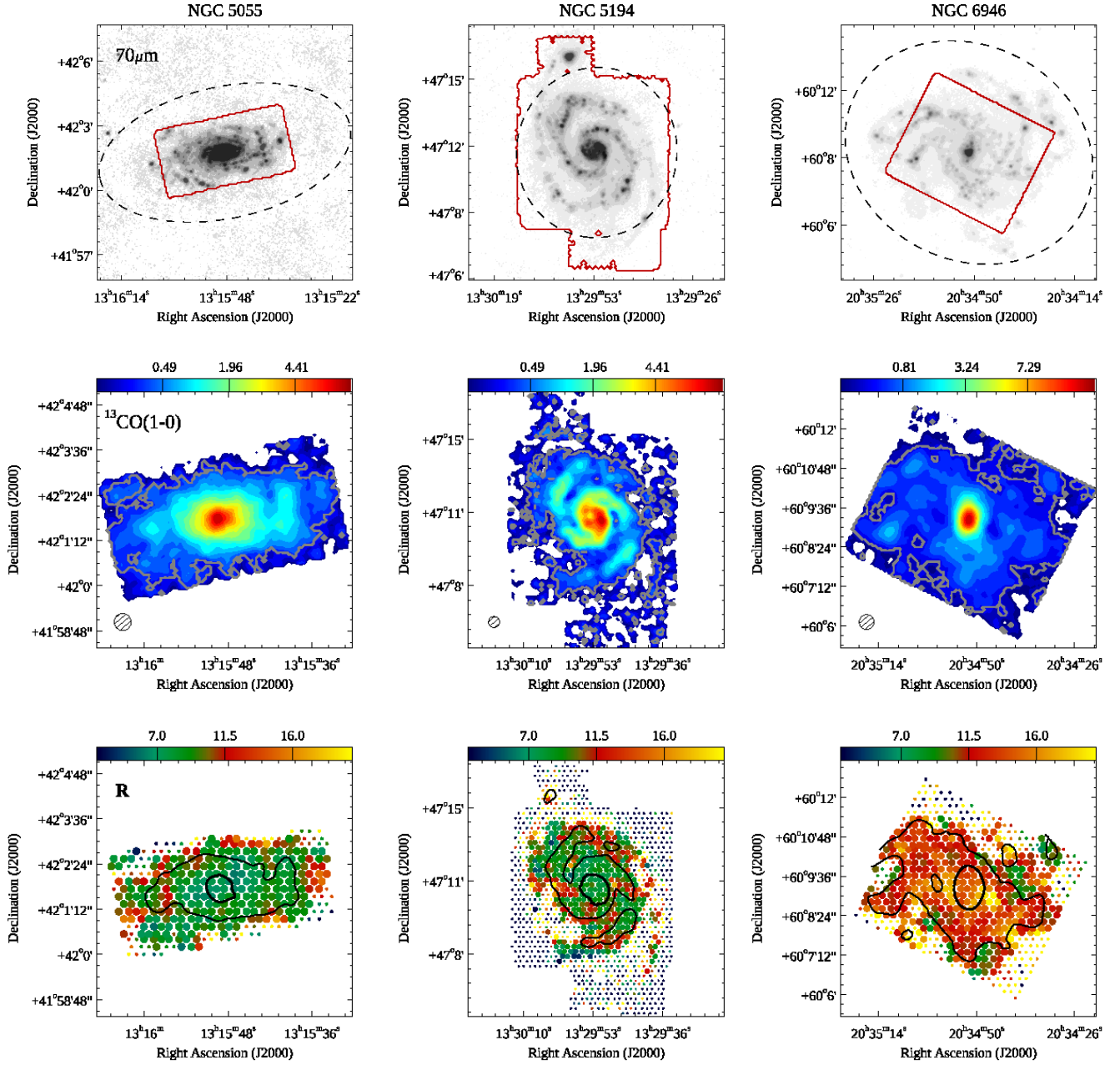
Figure A1 – *continued*
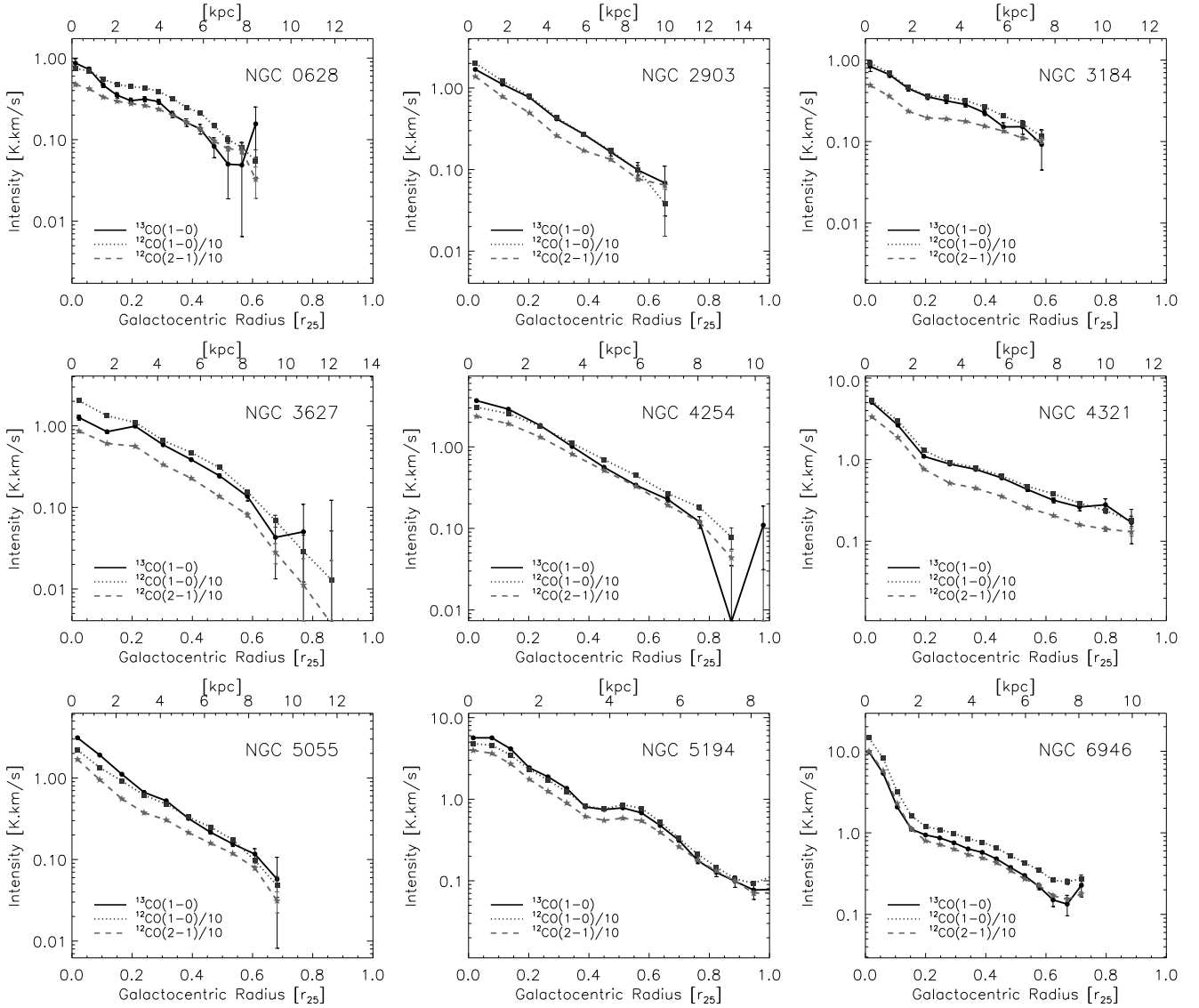
Figure A1 – *continued*

Figure A2. Profiles of the ^{13}CO(1-0), ^{12}CO(1-0) and ^{12}CO(2-1) intensities as a function of galactocentric radius.

less well peaked, probably because the dynamic range in the ratios is not very large.

Σ(SFR)/CO(1-0) and 1/$\mathfrak{R}$: The same two tests as described above are performed for Σ(SFR)/CO(1-0) instead of CO(2-1)/CO(1-0). Here, we find for all galaxies that the peak of the distribution of the standard deviations in the simulated Σ(SFR)/CO(1-0) values is systematically lower by a factor of ~2 compared to the observed standard deviation. Hence the scatter in the observed Σ(SFR)/CO(1-0) values is physical.

The second test indicates that the correlation coefficients and slope values between $\mathfrak{R}$ and Σ(SFR)/CO(1-0) reported in Fig. 4d are also robust. The distribution of the slopes is more peaked than with CO(2-1)/CO(1-0).

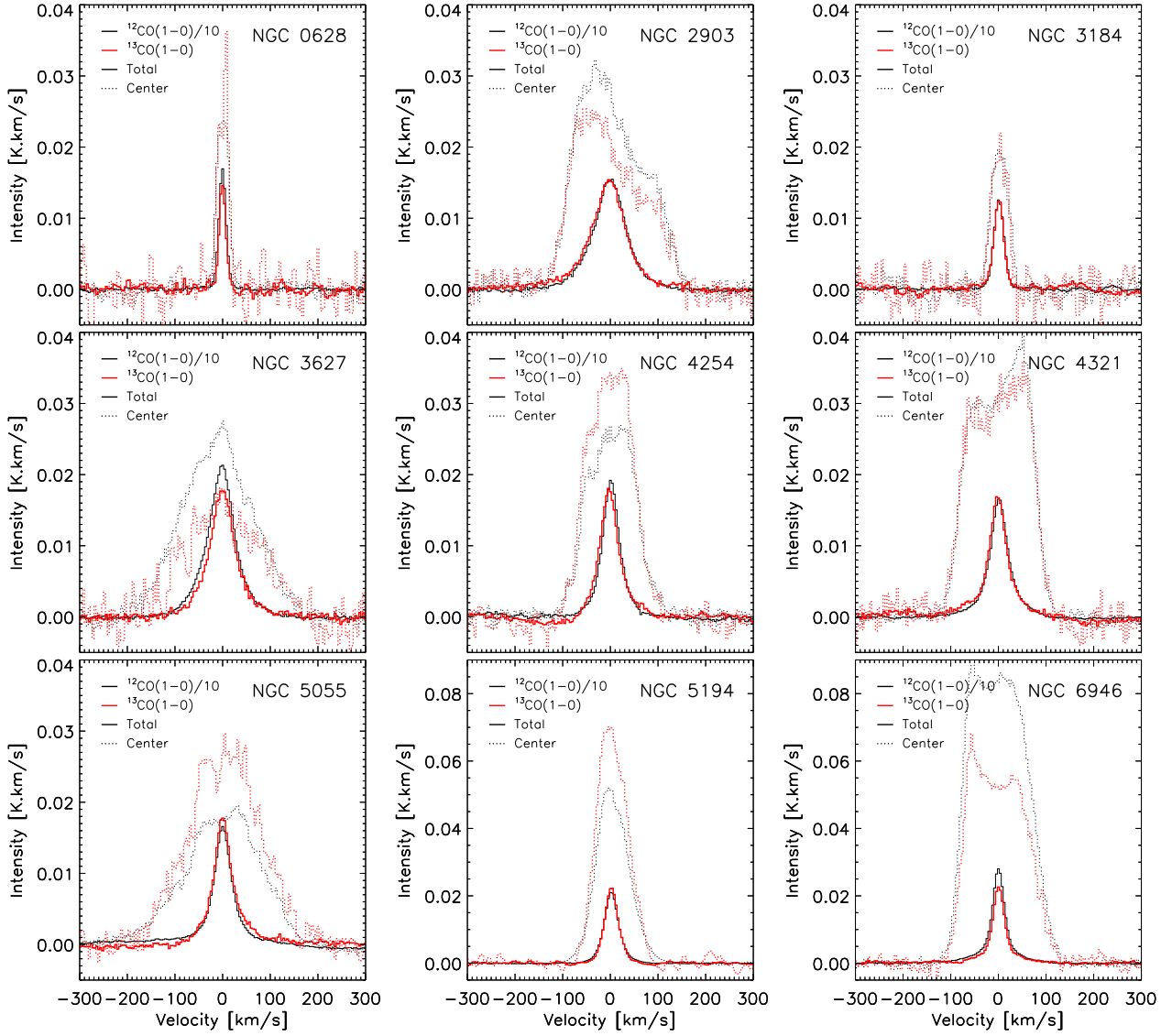This paper has been typeset from a TEX/LATEX file prepared by the author.

Figure A3. Stacked spectra of ^{13}CO(1-0) and ^{12}CO(1-0) over entire galaxies and in the galaxy centres.